Sliding or stumbling on the staircase: numerics of ocean circulation along piecewise-constant coastlines

Antoine-Alexis Nasser [1,2], Gurvan Madec [1,2], Casimir de Lavergne [2], Laurent Debreu [1], Florian Lemarié [1], Eric Blayo [1]

[1]University of Grenoble Alpes, INRIA, CNRS, Grenoble INP, LJK, 38000 Grenoble, France
[2]LOCEAN Laboratory, Sorbonne University-CNRS-IRD-MHNM, Paris F-75005, France

Key Points:

- Circulation within an idealized square basin is insensitive to mesh orientation and coastline indentation provided that physical convergence is achieved.
- Indented coastlines behave as straight and slippery when a true mirror boundary condition is imposed on the flow.
- The impact of a protruding corner in the coastline is faithfully simulated with exclusive implementation of impermeability conditions.

Corresponding author: Antoine-Alexis Nasser, `antoine-alexis.nasser@inria.fr`

Abstract

Coastlines in most ocean general circulation models are piecewise constant. Accurate representation of boundary currents along staircase-like coastlines is a long-standing issue in ocean modelling. Pioneering work by Adcroft and Marshall (1998) revealed that artificial indentation of model coastlines, obtained by rotating the numerical mesh within an idealized square basin, generates a *spurious form drag* that slows down the circulation. Here, we revisit this problem and show how this spurious drag may be eliminated. First, we find that *physical* convergence (i.e. the main characteristics of the flow are insensitive to the increase of the mesh resolution) allows simulations to become independent of the mesh orientation. An advection scheme with a wider stencil also reduces sensitivity to mesh orientation from coarser resolution. Second, we show that indented coastlines behave as straight and slippery shores when a true mirror boundary condition on the flow is imposed. This finding applies to both symmetric and rotational-divergence formulations of the stress tensor, and to both flux and vector-invariant forms of the equations. Finally, we demonstrate that the detachment of a vortex flowing past an outgoing corner of the coastline is faithfully simulated with exclusive implementation of impermeability conditions. These results provide guidance for a better numerical treatment of coastlines (and isobaths) in ocean general circulation models.

Plain Language Summary

Most numerical models of the ocean represent real coastlines or undersea land-forms as a staircase-like boundary. This approximation is necessitated by the size and square shape of model grid cells, together with the need to separate ocean cells from land cells. Pioneering work by Adcroft and Marshall (1998) revealed that the resultant artificial indentations of the boundary exert a spurious drag that systematically impedes coastal flow. Here, we revisit this problem and show how this spurious drag may be eliminated. First, we find that having sufficiently fine spatial resolution to resolve the physical processes allows the model to be insensitive to coastal indentation. Second, we show that staircase-like coastlines behave as straight and slippery shores when a true mirror condition on the flow is imposed at the coast. Finally, we show how to faithfully simulate the natural detachment of a vortex past an outgoing corner of the coastline. In a nutshell, these results provide guidance for a better numerical representation of marine land-forms in numerical ocean models.

1 Introduction

Drawing the separation between land and ocean grid cells is a pre-requisite to building any ocean model configuration. This task requires non-trivial coarse-graining of the target (observed or idealized) bathymetry. Consider the example of the coastline in an ocean general circulation model (OGCM) with a structured numerical mesh (Fig. 1). The real coastline typically needs to be approximated by a piecewise constant boundary. This approximation involves the removal of sub-grid-scale features of the real coast, the sharpening of real bends into corners, and the creation of artificial steps due to misalignment between the real coastline and the numerical mesh (Fig. 1). This transformation of the real coastline carries important consequences for the simulated boundary currents, and therefore for the simulated large-scale circulation (Ezer, 2016). These consequences depend not only on the design of the model coastline, but also on other numerical choices such as lateral boundary conditions (Adcroft & Marshall, 1998; Shchepetkin & O'Brien, 1996). However, little guidance currently exists to make the most appropriate numerical choices for the chosen application, and it is often unclear to what extent the model boundary behaves as the originally intended coastline.

Using an idealized square basin configuration and various orientations of the numerical mesh, Adcroft and Marshall (1998) (hereafter AM98) first pointed out that artificial indentation of a shoreline systematically causes a *spurious form drag* that slows down the coastal flow. AM98 showed that this drag depends on the numerical formulation of diffusive stresses but always exists, including when a 'free slip' boundary condition is implemented. Subsequent investigations within similar configurations showed that the response of the flow to staircase-like coastlines depends on the advection and diffusion schemes (Dupont et al., 2003). These studies also suggested that the spurious drag may persist at higher resolution because coastal steps increase in number as they become smaller (Adcroft & Marshall, 1998; Dupont et al., 2003). Griffiths (2013) argued that the adverse effects of an indented coastline could be handled by implementing the right impermeability condition corresponding to the real coastline. However their findings apply only to travelling Kelvin waves, and it remains unclear how the long-standing issue of spurious form drag should be addressed in OGCMs.

The response to an isolated, large-scale bend in the coastline also deserves attention because real swerves of the shoreline can have pronounced impacts on boundary currents (Magaldi et al., 2008; Warner & MacCready, 2009), and because such swerves may be sharpened in their discrete model representation. Deremble et al. (2016) showed that an outgoing corner in the coastline induces retroflection of a coastal stream. Their findings echo those of Dupont and Straub (2004), who varied the curvature of a wavy wall configuration and found that opposite vorticity filaments were created at the coastal tips and caused detachment of the flow. In both studies, only some numerical formulations enable to capture the expected physical behaviour. The reasons for this strong sensitivity to numerical formulations are not fully elucidated.

Here, we address these questions using idealized model configurations. We first reproduce the configuration of AM98 (section 2) and demonstrate that the circulation is insensitive to the mesh orientation—and related coastline indentation—provided that the model is *physically* converged (section 3). Next, we expose how a *true* mirror boundary condition on the flow renders the indented coastline as slippery as a straight, free-slip frontier (section 4). The numerical representation of an isolated, large-scale step in the coastline is investigated in section 5 using the configuration of Deremble et al. (2016). We summarize our findings and recommendations in section 6.

2 Methods

2.1 Configuration

We consider the same problem as AM98: a shallow water model with reduced gravity is solved in a square basin of size $L = 2000\,\mathrm{km}$. An anticyclonic wind stress $\tau = (-\tau_0 \cos(\pi y/L), 0)$ is forcing the active layer. The coordinate system (x, y) has its origin in the lower left corner of the square basin. Equations in vector invariant form read

$$\partial_t h + \mathrm{div}\,(h\mathbf{u}) = 0 \tag{1}$$

$$\partial_t \mathbf{u} + \left(\frac{f+\zeta}{h}\right)\mathbf{k}\times h\mathbf{u} + \nabla\frac{1}{2}(\mathbf{u}.\mathbf{u}) = -g'\nabla h - r\mathbf{u} + \mathbf{D}_\nu + \frac{\tau}{\rho_0 h} \tag{2}$$

where h is the active layer thickness, $\mathbf{u} = (u, v)$ represents the horizontal velocity vector, $\zeta = \mathbf{k}.(\nabla\times\mathbf{u})$ the relative vorticity, $\mathbf{k}$ the vertical unit vector, f the Coriolis parameter, g' the reduced gravity, r the friction coefficient, $\mathbf{D}_\nu$ the diffusion term and ρ_0 the density.

Two formulations of the diffusion term ($\mathbf{D}_\nu$ where ν is the lateral viscosity) are considered, that will lead to different discretisations: the rotational-divergence (hereafter called 'rot-div') form (Madec et al., 1991) and the symmetric form (Griffies & Hallberg, 2000). The rot-div form is calculated as $\nabla(\nu\chi) - \frac{1}{h}\nabla\times(\nu h\zeta)$ where transport diver-

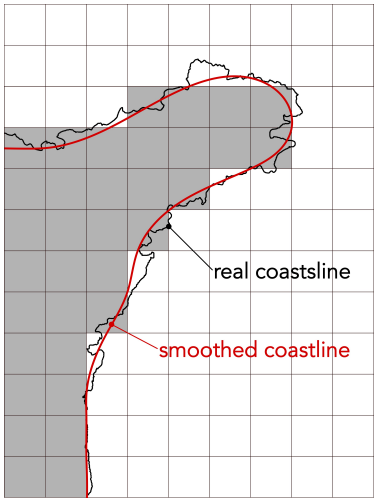

Figure 1. Schematic illustrating the coarse-graining of a coastline on a structured mesh. The real coastline (thin brown line) presents an infinite number of details that are too small, relative to the size of grid cells (thin black), to be represented by the numerical model. It must be averaged over at least two grid points to avoid noise generation, resulting in a smooth coastline (red curve). Then the land mask (grey cells) is defined from the projection of the smooth coastline onto the grid, creating artificial abrupt changes in coastline direction.

gence χ is defined as $\chi = \frac{1}{h}\big(\partial_x(hu) + \partial_y(hv)\big)$. The symmetric form is expressed instead as $\frac{1}{h}\nabla\cdot(\nu h\sigma_{sym})$ (Gent, 1993) where

$$\sigma_{sym} = \begin{pmatrix} D_T & D_S \\ D_S & -D_T \end{pmatrix} \qquad \begin{matrix} D_T = \partial_x u - \partial_y v \\ D_S = \partial_x v + \partial_y u \end{matrix} \tag{3}$$

A viscous boundary condition (see section 2.3) is applied at the wall of the basin by enforcing the values of χ and ζ in the 'rot-div' form and D_S and D_T in the symmetric form. In the discrete form, the same viscous boundary condition can thus be written differently depending on the formulation of $\mathbf{D}_\nu$.

We will also perform simulations using the flux form of the shallow water equations. In this case, equation (2) rewrites as

$$\partial_t(h\mathbf{u}) + \nabla\cdot(h\mathbf{u}\otimes\mathbf{u}) + f(\mathbf{k}\times h\mathbf{u}) = -g'h\nabla h - rh\mathbf{u} + h\mathbf{D}_\nu + \frac{\tau}{\rho_0} \tag{4}$$

2.2 Numerical discretisation

We use for the numerical simulations the shallow water option (SWE) introduced in the version 4.2 of the NEMO general circulation model (Madec & NEMO System Team, 2022). The initial state is at rest with $h_0 = 500\,\mathrm{m}$ the uniform thickness of the active layer. Experiments are integrated over 25 years to achieve a steady state on h. All the simulations presented here use the Leap Frog Robert-Asselin time-stepping scheme (Leclair & Madec, 2009). In contrast, AM98 used the third order Adams-Bashforth (III) scheme. We do not expect the *spurious form drag* to be sensitive to the order of accuracy of the time-stepping scheme. We performed sensitivity tests with the third order Runge-Kutta method and found no noticeable differences in the equilibrium solutions (not shown).

Following AM98, we employ a Cartesian mesh with uniform resolution. Spatial resolution will be varied from 1/4° to 1/32°. In the reference case, the mesh is aligned with

the edges of the square basin, so that the model coastlines are perfectly straight (Fig. 2a). In the rotated cases, the mesh is oriented at some angle (up to 45°) with respect to the physical coastline, so that steps punctuate the model coastlines (Fig. 2b). Hence, the comparison of aligned and misaligned cases allows us to assess potential drag effects of artificial coastal indentation. Both physics (e.g., wind stress, Coriolis parameter) and grid-cell size are kept unchanged when the mesh turns in relation to the physical basin, so that only the shape of the model coastline changes. Physical and numerical parameters are similar to AM98 and listed in Appendix A.

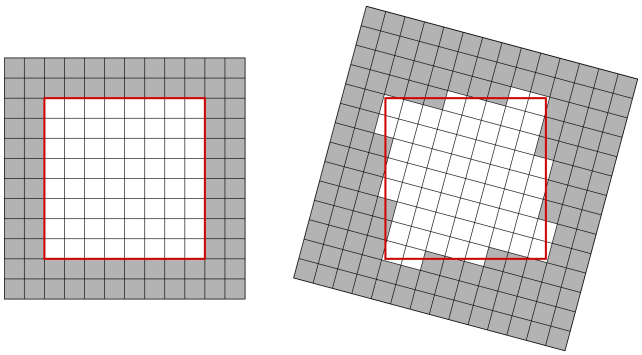

Figure 2. Effects of rotating the numerical mesh within an idealized square basin. The mesh is represented by the black lines. Land is shaded in grey, the oceanic domain in white. The red thick line represents the physical coastline. On the left, the grid is aligned with the basin. On the right, the mesh is rotated so that artificial steps appear in the model shoreline. This figure is adapted from AM98.

All the simulations solved in vector-invariant form and shown in this study use the potential-enstrophy conserving vorticity scheme (called ENS) (Sadourny, 1975), except in section 4.4 where we tested the scheme (called EEN) developed by Sadourny which conserves kinetic energy and—provided there is no divergence in the flow—potential enstrophy (Burridge & Haseler, 1977). Tests showed that solutions using the kinetic energy conserving advection scheme (called ENE) (Sadourny, 1975) behave very similarly to the ones shown here with the ENS scheme. Note that AM98 used the 'vorticity' scheme given by Bleck and Boudra (1986), which is similar to ENS except for the presence of the vertical scale factor h at the numerator and denominator in ENS (as required to effectively conserve a discrete expression of potential enstrophy (Sadourny, 1975)). Additional tests showed that 'vorticity' and ENS schemes yield solutions that are slightly different but behave similarly in the presence of staircase-like coastlines. The expression of the various discretisation schemes is given in Appendix B.

This configuration assumes an idealistic topography made of vertical walls and a flat bottom. However, the effective topography can be distorted by the traditional estimation of the thickness h at U, V and F boundary nodes. In the open ocean on a C-grid, h is naturally defined at the center of each cell and calculated as a two-point (or four-point) average at velocity (or vorticity) nodes, for discrete conservation of properties. At the boundary, using the same definition and averaging with masked h can be equivalent to imposing sub-grid-scale topography, and can reinforce topostrophy. Tests under ENS, ENE and EEN advection schemes showed that simulations are sensitive to the treatment of h at the boundary (not shown), especially with EEN. We chose to calculate boundary h as the masked average of the surrounding masked heights, in order to actually represent vertical walls.

2.3 Boundary condition

The system of equations (1)-(2) or (1)-(4) requires two horizontal boundary conditions to be well posed. The standard conditions on a solid wall consist of the impermeability condition $\mathbf{u}.\mathbf{n} = 0$, with $\mathbf{n}$ the coast-normal unit vector, and of a slipperiness condition that is a simplified representation of the effects of a viscous boundary layer.

AM98 considered two types of slipperiness condition (hereafter called *viscous boundary condition*): no-slip and free-slip. No-slip requires the tangential speed to be zero at the boundary which is $\mathbf{u}.\mathbf{t} = 0$, with $\mathbf{t}$ the coast-tangential unit vector. Combined with the impermeability condition ($\mathbf{u}.\mathbf{n} = 0$), no-slip thus entails $\mathbf{u} = 0$ at the border. By contrast, free-slip is the absence of shearing and hence dissipation at the coast. It is defined as the absence of coast-normal shear at the border $\partial\mathbf{u}/\partial\mathbf{n} = 0$ and can be interpreted as a mirror condition across the border, where virtual flow within land mirrors the oceanic flow.

It is possible to deduce from the viscous boundary condition the value of the vorticity at the boundary. In their section 2, Verron and Blayo (1996) write the vorticity at an impermeable boundary regular enough to define the local vectors $(\mathbf{n}, \mathbf{t})$:

$$\zeta = \left(\kappa\mathbf{u} - \frac{\partial \mathbf{u}}{\partial \mathbf{n}} \right).\mathbf{t} \tag{5}$$

with κ the local curvature of the coastline. When the coastline is straight (κ tends to 0), no-slip implies $\zeta = -(\partial\mathbf{u}/\partial\mathbf{n}).\mathbf{t}$ while free-slip reduces to $\zeta = 0$. When dealing with a numerical model, depending on the numerical grid and discretisation schemes, the evaluation of a quantity on a grid-point near the boundary may require the use of another quantity at the boundary. It is for instance the case of ζ in the non-linear term in equation (2), and the case of the rot-div formulation of the diffusive term. The boundary conditions therefore provide this information.

3 The need for physical convergence

3.1 Influence of resolution

The numerical parameters chosen by AM98 are those of an eddy-permitting OGCM: horizontal resolution is 1/4°, corresponding to a grid spacing $\Delta x = \Delta y = 25$ km. At this resolution, neither the internal radius of deformation R nor the boundary layers are properly resolved throughout the basin (Hallberg, 2013). Indeed, in the initial state, the deformation radius is about 35 km at the northern boundary, so that $\Delta x \sim R$. It is therefore expected that increasing spatial resolution while keeping the same values for physical parameters (i.e. viscosity ν and friction r) will give solutions that differ from the reference solution of AM98.

Figure 3 shows the steady solution using the vector-invariant form of equations with the ENS advection scheme, the rot-div stress tensor and the free-slip boundary condition. From top to bottom, spatial resolution increases successively from 1/4° to 1/8°, 1/16° and 1/32°. The mesh is either aligned with the coastline (left column) or rotated by 45° (right column). The 45° angle creates an artificially indented coastline, as illustrated in Figure 2. Shading and isolines depict the layer thickness h. In all cases, we obtain an anticyclonic (clockwise) circulation composed of two connected cells: a relatively weak Sverdrup interior intensified at the western boundary in the southern 1500 km of the domain, and an inertial recirculation sub-gyre confined to the northernmost 500 km. We find that some high resolution simulations vacillate in the eastern part of the recirculation cell; that is, the simulated flow displays an oscillatory behaviour in this region over a timescale of about 18 months. Such vacillation is thought to occur in a very restrained parameter range (Holland & Haidvogel, 1981). To ensure consistent comparisons, all shown free-slip solutions are averaged over the final 5 years.

Panels (a) and (b), corresponding to a resolution of 1/4°, reproduce the results of AM98. At this resolution, the inertial recirculation cell extends all the way to the eastern boundary when the mesh is aligned with the physical coastline, whereas it occupies only the western half of the basin when the mesh is rotated by 45°. Hence, the free-slip circulation seems to dwindle as the mesh turns. However, the latter statement is no longer true with a fine spatial resolution. At 1/32°, the two solutions are virtually identical (Fig. 3g,h). As apparent in the evolution of the shape and maximum of the northern recirculation, both aligned (Fig. 3a,c,e,g) and turned (Fig. 3b,d,f,h) solutions appear to tend toward the same state. Besides, solutions at 1/16° look very similar to the ones obtained at 1/32° meaning that the solutions are *physically* converged from 1/16° (i.e. the main characteristics of the flow are almost insensitive to the increase of the mesh resolution).

The inertial recirculation sub-gyre is the most sensitive feature to resolution and mesh orientation. Hence, we choose to quantify the model sensitivity to the rotation and resolution of the grid using two diagnostics: the zonal extension of the inertial cell, and its overall intensity (calculated as the maximum of the active layer thickness within this cell). Figure 4 compares these diagnostics at different orientations of the mesh as a function of resolution. The extension (Fig. 4a) and intensity (Fig. 4b) of the rotated (dark blue dotted line) and aligned (red dotted line) solutions are very similar at 1/16° and continue to get closer at the finest resolutions. Both characteristics rapidly tend toward those of the 1/48° solution.

Figures 3 and 4 thus demonstrate that (i) the reference aligned solution should be the one obtained at 1/16° resolution (Fig. 3e - now taken as the reference) instead of 1/4° (Fig. 3a); and (ii) the simulated circulation is insensitive to staircase-like coastlines provided that the model is physically converged.

3.2 Preserving 1/4° staircase steps

When increasing spatial resolution, the size of the coastal steps decreases as their number increases along the coastline. Is the insensitivity to mesh orientation at high resolution due to the smaller step size? To answer this question, we performed 1/16° simulations with exaggerated coastal indentation (identical to its shape at 1/4° resolution). In this way, we maintain the broken aspect of the shoreline unchanged while reducing the grid spacing. We find that the final free-slip solution (Fig. 5a) is insensitive to the larger steps: it is almost identical to the reference aligned solution (Fig. 3e). Hence, physical convergence allows the simulated circulation to be insensitive to mesh orientation and coastal indentation, irrespective of the size of coastal indents.

3.3 Condition for physical convergence

The zonal development of the northern recirculation cell results from a non-linear interaction between the sub-gyre and its mirror recirculation induced by the free-slip boundary condition (e.g. Fig. 1 of Cessi (1991)). The northern region is also where the deformation radius is the smallest. This radius is about 35 km at the northern boundary in the initial state and it decreases over time because the westerly wind stress causes upwelling along the northern coast (thus shrinking h). Therefore, the deformation radius near the northern boundary is never properly resolved on a 1/4° mesh. To assess whether resolution of the deformation radius along the northern frontier is key to obtain physical convergence, we performed experiments where the aligned, 1/4° mesh is refined in a narrow northern band. Specifically, we reduce the meridional grid spacing from 1/4° 300 km offshore to 1/16° at the northernmost grid cells.

Figure 5b shows that refining the meridional grid spacing near the northern boundary contracts the inertial recirculation sub-gyre (compare with Fig. 3a). Local grid refinement thus suffices to bring this recirculation cell closer to the physically converged

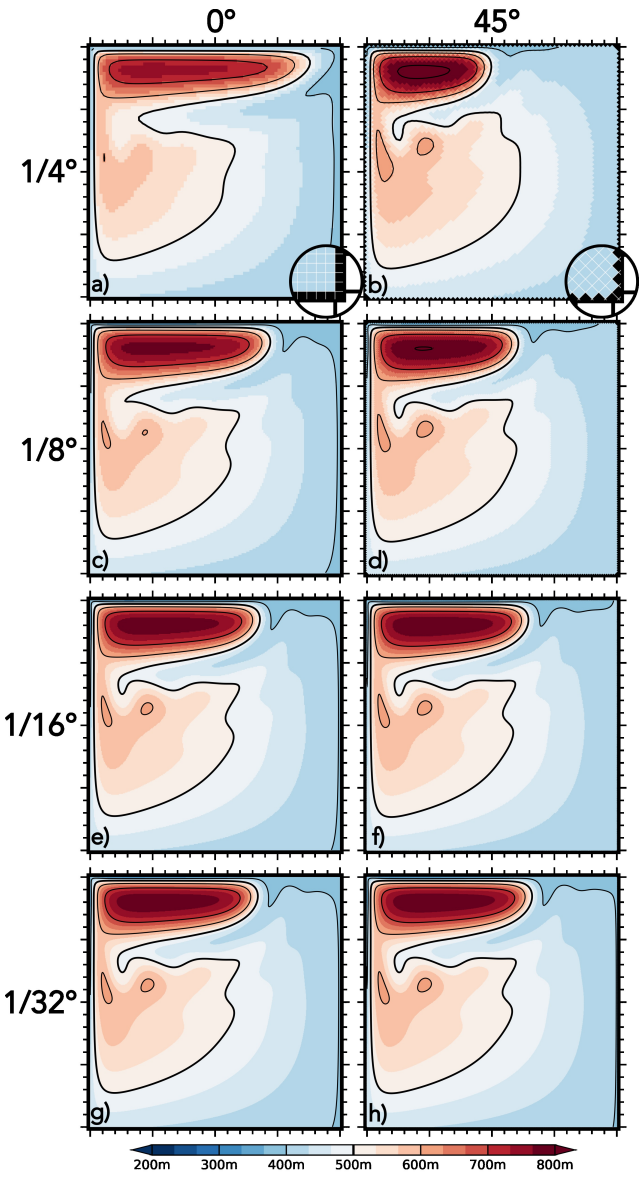

Figure 3. Free-slip solutions solved in vector-invariant form under ENS using the rot-div stress tensor. Shading and isolines (in black) depict the active layer thickness h (isoline 500 m is thickened). x and y main ticks are 500 km apart. In the left column (a,c,e,g), the mesh is aligned with the borders of the basin. In the right column (b,d,f,h), the mesh is turned at 45° relative to the borders, as illustrated in the bottom-right zooms. The spatial resolution increases from top to bottom: (a,b) 1/4°, (c,d) 1/8°, (e,f) 1/16° and (g,h) 1/32°.

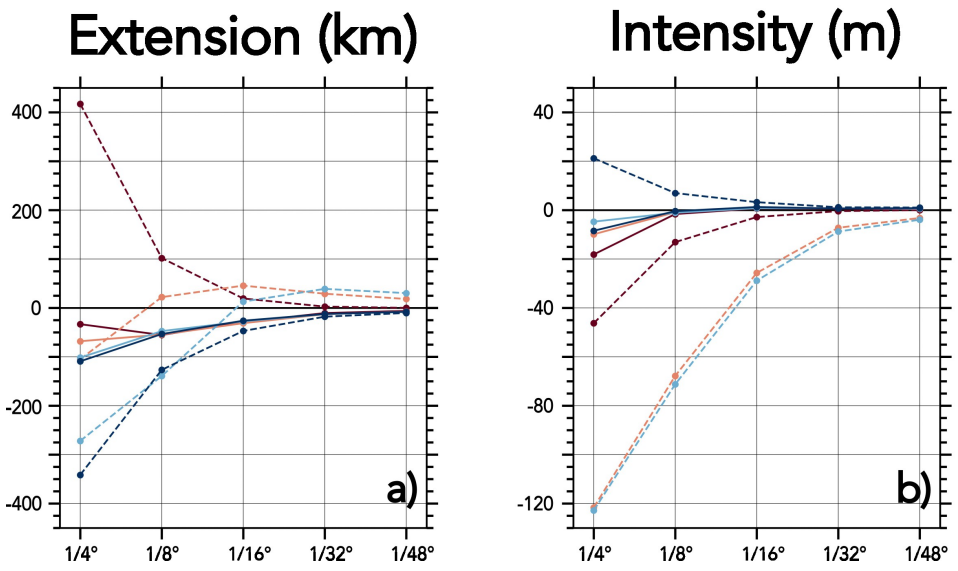

Figure 4. Extension and intensity of the free-slip solutions solved in vector-invariant form using the rot-div stress tensor. The extension of the inertial recirculation cell (a) is the zonal length (in km) measured between the two most distant points on the 500 m isoline of upper-layer h. Its intensity (b) is the maximum (in m) of the active layer thickness h. Both quantities are plotted as a function of mesh resolution, and are shown as a difference relative to values from the finest aligned solution (1/48°) resolved under ENS (these values are 1311 km and 794 m). Dotted lines (solid lines) depict solutions solved under ENS (EEN) scheme. The sequence of colors (red, orange, light blue and dark blue) marks the orientation of the mesh (aligned, 10°, 30° and 45°, respectively).

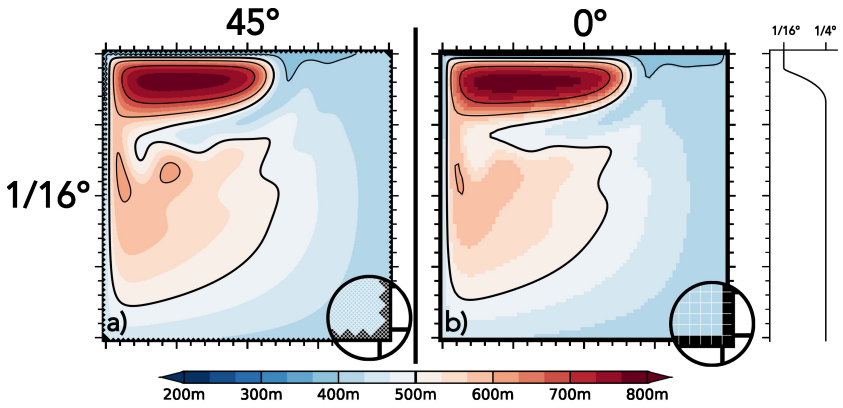

Figure 5. Free-slip solution solved in vector-invariant form under ENS using the rot-div stress tensor. Shading and isolines (in black) depict the active layer thickness h (isoline 500 m is thickened). x and y main ticks are 500 km apart. a) The mesh is oriented at 45° and the spatial resolution 1/16° but coastal steps remain of size corresponding to 1/4° resolution. b) The mesh is aligned and uniformly at 1/4° except within 300 km of the north coast where the meridional spatial resolution is refined from 1/4° to 1/16° (as illustrated in the right-end panel).

solution (Fig. 3e) than to the initial 1/4° solution (Fig. 3a). Analogous sensitivity tests with local mesh refinement close to the western, southern or eastern coast showed very little impact on the solution (not shown). Resolving the northern deformation radius, hence the mirror interaction at the north boundary, appears to be the key ingredient for physical convergence. We infer that a minimum of four grid points per deformation radius is necessary.

3.4 No-slip boundary condition

All experiments up to here have been conducted using the free-slip boundary condition. The no-slip boundary condition may be expected to generate weaker circulation cells and weaker sensitivity to mesh orientation (AM98). Figure 6 shows no-slip solutions using aligned (left) and 45°-rotated (right) meshes, at 1/4° (top) and 1/16° (bottom) resolution. Under no-slip, there is no large recirculation cell in the northern part of the domain and the zonal transport is two times weaker there. Instead, no-slip solutions converge in time toward an oscillating small gyre nestled in the north-west corner. At 1/4° resolution, a 45° rotation of the mesh causes the small gyre to shift south by about 200 km (Fig. 6a,b). At 1/16° resolution, this sensitivity vanishes (Fig. 6c,d). Hence, insensitivity to mesh orientation is again achieved provided that spatial resolution is sufficiently fine. The same conclusion holds when no-slip is applied in the symmetric stress tensor formulation (not shown).

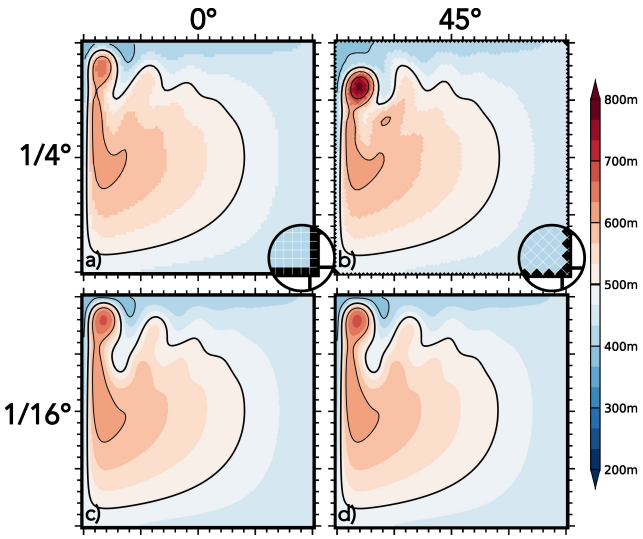

Figure 6. No-slip solutions solved in vector-invariant form under ENS with the rot-div stress tensor. Shading and isolines (in black) depict the active layer thickness h (isoline 500 m is thickened). x and y main ticks are 500 km apart. In the left column, the mesh is aligned with the physical coastline. In the right column, the mesh is 45°-turned. Spatial resolution is 1/4° in the top row and 1/16° in the bottom row. Because the final state steadily oscillates over periods of roughly 5 months (linked to the generation of Rossby waves), the shown solution is extracted by averaging over many periods.

4 True mirror boundary condition achieves slipperiness

4.1 Symmetric stress tensor

A major caveat pointed out in AM98 is the extreme sensitivity to mesh orientation of free-slip solutions that resort to the symmetric viscous stress tensor. Figure 7 shows solutions using the free-slip boundary condition and the symmetric stress tensor. When the mesh is aligned with the physical coastline (Fig. 7a,d), the model behaviour is qualitatively similar to what was obtained using the rot-div stress tensor (Fig. 3a,e). However, when the mesh is rotated by 45° (Fig. 7b,e), both coarse and fine solutions change starkly and resemble no-slip solutions (Fig. 6) as pointed out in AM98. Hence, the free-slip boundary condition combined with the symmetric stress tensor appears to act as no-slip when the mesh is oriented at 45°, which suggests that its implementation is not suitable. We next examine how to recover a true free-slip condition on the 45°-turned mesh using the symmetric tensor.

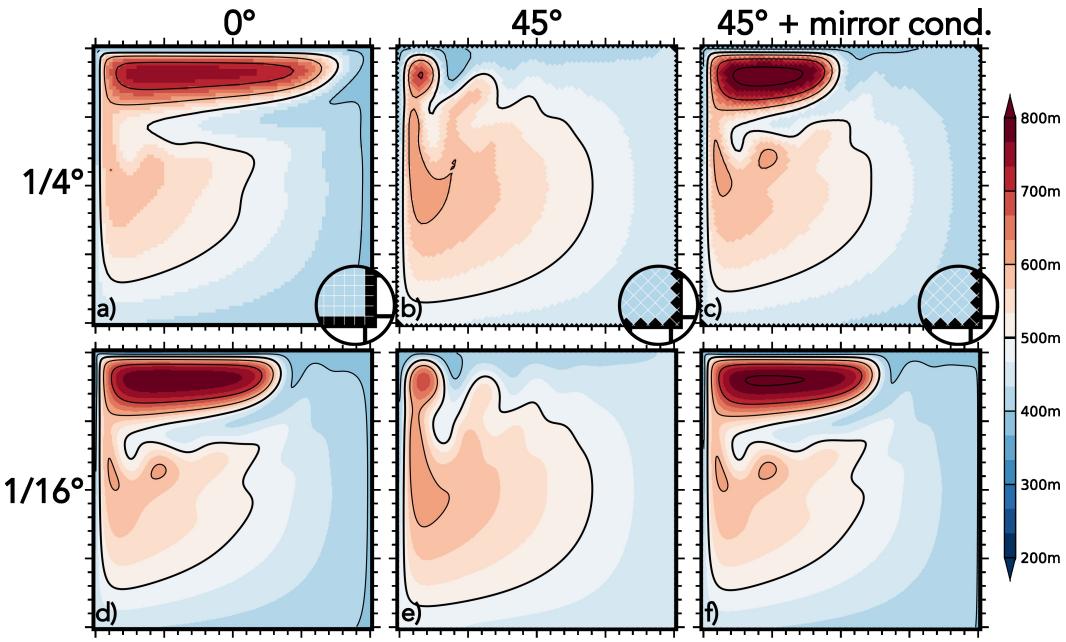

Figure 7. Free-slip solutions solved in vector-invariant form under ENS using the symmetric stress tensor. Shading and isolines (in black) depict the active layer thickness h (isoline 500 m is thickened). x and y main ticks are 500 km apart. Spatial resolution is 1/4° in the top row and 1/16° in the bottom row. In the left column, the mesh is aligned with the physical coastline. In the middle and right columns, the mesh is 45°-turned. The first two columns use the traditional free-slip implementation in the symmetric tensor ($D_S = 0$), whereas the third column uses the mirror condition proposed in equations (6) and (7).

When the mesh is not aligned with the physical coastline, the original straight boundaries become broken or indented in the model. To faithfully represent boundary flows, boundary conditions should be written with respect to the original, physical land-ocean frontier. For example, at 45°, the physical shoreline goes through T and F nodes (Fig. 8). A free-slip condition is a mirror condition at the coast (e.g., Shchepetkin and O'Brien (1996)). Therefore, we should set virtual flows on 'ghost nodes' (AM98), within land grid cells, that are symmetric to the ocean flows with respect to the physical shoreline. These virtual velocities are only used to evaluate the lateral friction term along the border. The

Table 1. Proposed viscous boundary conditions for a uniform and 45°-turned mesh. The table gives the modifications of quantities used in either tensor to be implemented at the coast, relative to the trivial case of zero virtual velocities. The top row describes quantities of the rot-div tensor while the bottom row describes quantities of the symmetric tensor, as defined in section 2.1.

	free-slip	no-slip
$\sigma_{\zeta,D}$	$\zeta \times 0$	$\zeta \times 2$
	$\chi \times 2$	$\chi \times 0$
σ_{sym}	$D_S \times 2$	$D_S \times 0$
	$D_T \times 0$	$D_T \times 2$

example of a western coastline is illustrated in Figure 8. In this case, the mirror condition writes

$$\widetilde{u}_{i,j+1} = v_{i+1,j} \tag{6}$$
$$\widetilde{v}_{i,j} = u_{i,j} \tag{7}$$

where the tilde is used to denote inland virtual velocities. It is the same condition as proposed by Griffiths (2013) in the context of Kelvin waves. Both anti-diagonal (D_S or ζ) and diagonal (D_T or χ) rates of deformation, defined at vorticity and tracer points respectively, are then deduced from this mirror condition. In particular, for a uniform grid spacing Δx ($= \Delta y$), we have

$$(D_S)_{i,j} = \frac{1}{\Delta y}\left(\widetilde{u}_{i,j+1} - u_{i,j}\right) + \frac{1}{\Delta x}\left(v_{i+1,j} - \widetilde{v}_{i,j}\right) = \frac{2}{\Delta x}(v_{i+1,j} - u_{i,j+1}) \tag{8}$$

Hence, D_S is not zero at the tips of the coastal steps, but instead doubled compared to the value obtained with zero virtual inland velocities. This is contrary to the traditional implementation of free-slip in the symmetric tensor, which sets $D_S = 0$ at the boundary. $D_S = 0$ is the correct condition when the numerical and physical shorelines perfectly coincide but fails when they are misaligned.

The no-slip condition can be defined following the same rationale, by setting inland virtual velocities as the opposite to their oceanic mirrors:

$$\widetilde{u}_{i,j+1} = -v_{i+1,j} \tag{9}$$
$$\widetilde{v}_{i,j} = -u_{i,j} \tag{10}$$

The proposed free-slip and no-slip conditions for a 45°-turned mesh and either stress tensor are summarized in Table 1. Note that we could have considered that the physical shoreline goes through (U,V) nodes, as AM98, instead of (T,F) nodes. In this case, the mirror condition requires a slightly more complex interpolation of the virtual velocities.

We implemented the proposed free-slip condition in the symmetric stress tensor and assessed the impact on the equilibrium solution with a 45°-turned mesh (Fig. 7c,f). In contrast to previous results which relied on the standard free-slip boundary condition (Fig. 7b,e), a true free-slip circulation is simulated with a northern recirculation cell that extends roughly to the middle of the basin. The solutions in Figure 7c,f are very similar to those previously obtained with the rot-div tensor (Fig. 3b,f). Our simulations thus

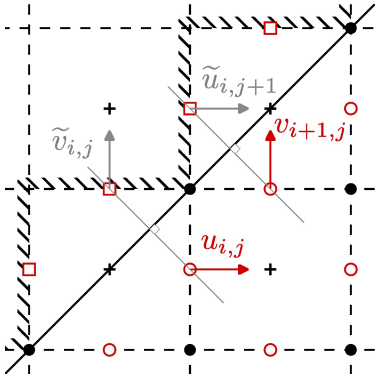

Figure 8. Schematic presenting a mirror condition on the western coastline. Land grid cells are located west of the black hatching. The original, physical coastline, goes through the diagonals of the cells and is drawn in solid black. Red circles locate velocity points, black disks locate vorticity points (F nodes) and black crosses height points (T nodes), as is standard for a C-grid. Red squares mark boundary nodes or 'ghost nodes' where virtual velocities are defined. Example oceanic velocities are shown by red arrows, mirrored by the virtual velocities shown with grey arrows.

confirm that the traditional way of applying free-slip in the symmetric tensor ($D_S = 0$) is not suitable when the mesh is misaligned with the coastline.

We stress that setting only D_S at the tips of steps is insufficient to obtain a true free-slip solution (not shown). Boundary conditions on both D_S and D_T are necessary to make the indented coastline slippery using the symmetric tensor. In contrast, cancelling only ζ in the rot-div tensor proved to be enough to achieve slipperiness; doubling χ only brought minor changes. Since the condition $\zeta = 0$ at the coast was already implemented in the experiments described in section 3, a correct free-slip behaviour was simulated.

4.2 Flux-form equations

All numerical experiments documented above were solved in vector-invariant form (Eq. 2). How slippery are staircase-like coastlines in a model solved in flux form (Eq. 4)? Figure 9 shows the steady flux-form solutions on aligned (Fig. 9a,d) and 45°-turned (Fig. 9b,c,e,f) meshes at 1/4° (top row) and 1/16° (bottom row) resolution, using the rot-div stress tensor. Figure 9a,d reveals the same contraction of the northern recirculation cell with increasing resolution as found previously (Fig. 3a,e) on the aligned mesh. However, when the mesh is turned and the coastline becomes indented, solutions become akin to no-slip: a small gyre is nestled in the northwest corner in an oscillatory steady state (Fig. 9b,e).

By construction, there is no viscous boundary condition applied in flux-form advection, only the impermeability condition holds. The viscous boundary condition is free-slip and implemented in the rot-div stress tensor. Under such parameters, a coastal step tends to generate filaments of opposite vorticity that cause the coastal current to retroflect (Deremble et al. 2016; see also section 5). Therefore, solutions solved in flux-form are expected to be sensitive to the presence of steps, as retroflection dynamics hinder along-boundary flow.

To remedy this sensitivity to mesh orientation, we implemented the same mirror condition (Eqs. (6) and (7)) but in the advective trend, by enforcing velocities at the coast to satisfy this condition. The result is shown in Figure 9c,f for the 45°-turned mesh. We

obtain a sizeable inertial recirculation cell in the northern part of the basin, with zonal extensions close to the previous solutions (Fig. 3b,d,f,h and Fig. 7c,f). Hence, enforcing the free-slip condition in both the diffusive and advective terms makes staircase-like coastlines slippery, including with flux-form equations.

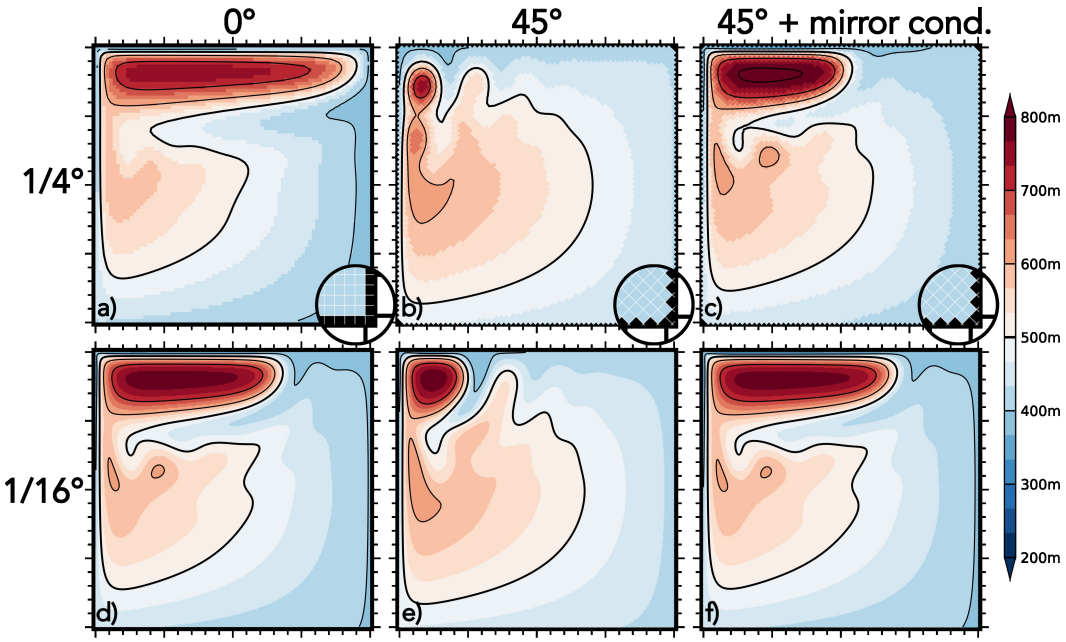

Figure 9. Free-slip solutions solved in flux form using the rot-div stress tensor. Shading and isolines (in black) depict the active layer thickness h (isoline 500 m is thickened). x and y main ticks are 500 km apart. Spatial resolution is 1/4° (top row) and 1/16° (lower row). In the first column (a,d), the mesh is aligned so the coastline is straight. Second and third columns (b,c,e,f) have the mesh rotated at 45°. In the third column, a mirror condition is enforced in the advective trend.

4.3 Intermediate angles

At 1/4° resolution, the fully indented coastline (Fig. 3b) leads to a solution closer to the converged solution (Fig. 3e-h) than does the straight coastline (Fig. 3a). At intermediate orientations of the mesh (strictly between 0° and 45°), the coastline counts fewer outgoing angles than at 45°, and a solution midway between the aligned and 45°-turned cases might be expected. In reality, intermediate angles generate solutions that depart much more from the converged solution (Fig. 10). Figure 10 uses the exact same numerical choices as Figure 3 except for the mesh orientation, which is either 10° (left column) or 30° (right column). At these orientations, the inertial recirculation cell expands toward the east between 1/4° and 1/16°, then contracts with resolution (Fig. 10). Solutions (not shown) performed on 1/48° mesh are not significantly different from the ones obtained on 1/32° mesh (Fig. 10g,h) meaning that physical convergence is reached near 1/32°. The curves plotted in Figure 4 for 10° (orange dotted line) and 30° (light blue dotted line) orientations confirm and quantify these results. Interestingly, the 1/48° solutions at intermediate angles depart from the aligned solution (Fig. 4): their recirculation cells are wider by about 30 km, and weaker by about 5 m. It is puzzling that different converged solutions seem to exist for different orientations; one might have expected that the same solution be reached across all orientations at very fine resolution.

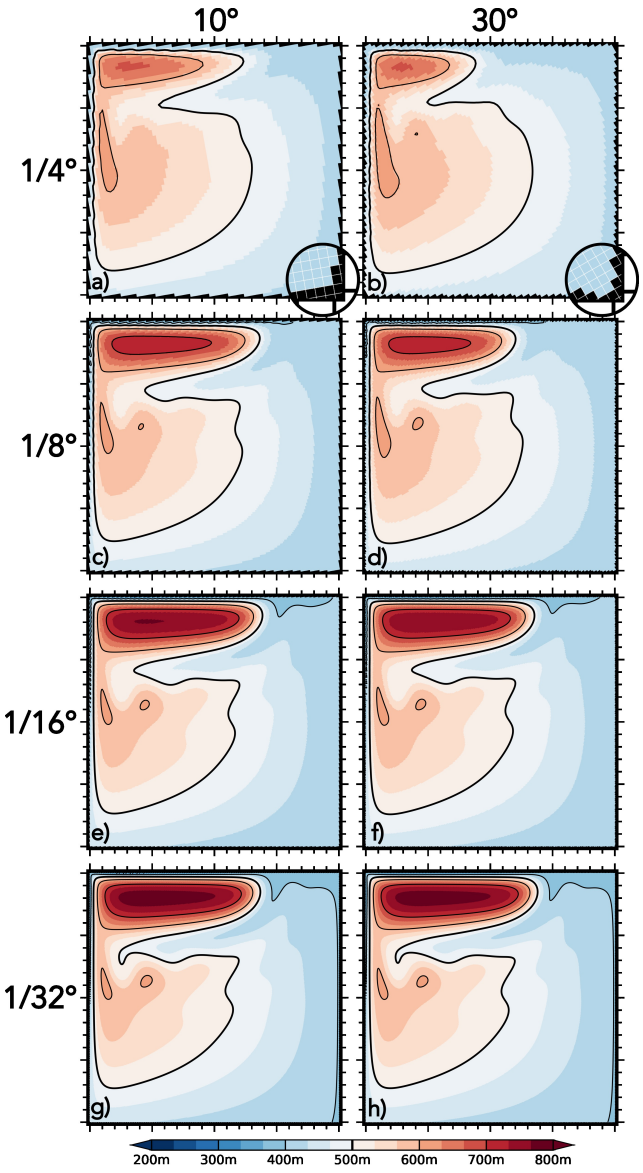

Figure 10. Free-slip solutions solved in vector-invariant form under ENS using the rot-div stress tensor. Shading and isolines (in black) depict the active layer thickness h (isoline 500 m is thickened). x and y main ticks are 500 km apart. The mesh orientation is 10° (left) and 30° (right). Spatial resolution increases from top to bottom: 1/4°, 1/8° , 1/16° and 1/32°.

Why do solutions at intermediate angles differ from their aligned and 45°-turned counterparts? Once the model is converged, dynamics inside the domain must be well captured independently of the orientation of the grid, so that differences are expected to lie at the borders. If the mesh is aligned (Fig. 11, left) or turned at 45° (Fig. 11, right), the physical coastline coincides with the F nodes of the C-grid and the free-slip condition $\zeta = 0$ exactly matches that of a straight coastline. At intermediate angles however, this condition is inaccurate because the free-slip boundary resulting in the model (red dotted line) is not straight but corrugated (Fig. 11, middle). Imposing $\zeta = 0$ on the tips does make artificial steps slippery yet does not achieve the true free-slip condition of a straight coastline. We expect that defining the free-slip condition with respect to a straight boundary would yield the same solutions and convergence rate as with the aligned mesh.

In other words, to accurately represent the free-slip condition, virtual inland velocities should be interpolated as the mirrors of the ocean flows with respect to the straight shoreline. Such a strategy would presumably allow to retrieve a true free-slip behaviour also with advection in flux form, and with the symmetric stress tensor, for any orientation of the mesh. We have not endeavoured such an interpolation at intermediate angles, for it is tedious and would not generalise to arbitrary (curved) physical shorelines. Instead, we suggest using more general techniques such as immersed boundary methods (Causon et al., 2000; Kirkpatrick et al., 2003; Ketefian & Jacobson, 2011).

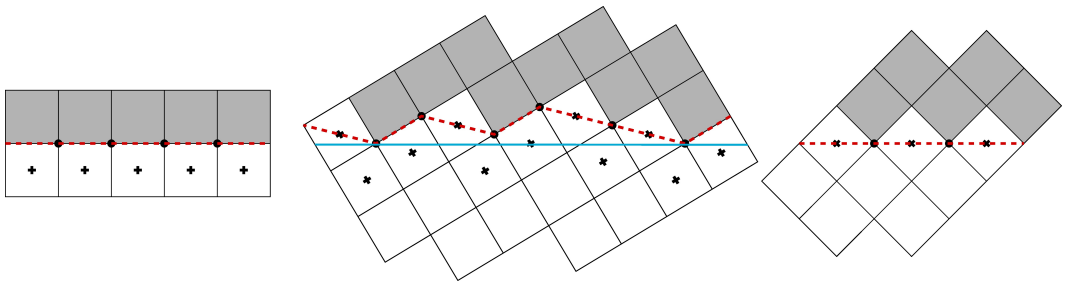

Figure 11. Representation on a C-grid of a straight shoreline with the piecewise constant approximation. The black disks are the vorticity (F) nodes and the crosses are the height (T) points. The numerical frontier (red dotted line) connects the vorticity nodes that influence the dynamics. In the aligned case (left) the numerical frontier occupies cell faces and joins F nodes so it coincides with a straight coastline. In a similar way, the numerical frontier in the 45°-turned case (right) goes through cell diagonals, hence intersecting F and T nodes. In the intermediate case (middle), the closest vorticity points to the targeted straight coastline (in blue) are not aligned, resulting in a slithering numerical frontier.

4.4 Benefit of wide stencils

Strictly speaking, the mirror condition should apply in each term of the equations. For example, on the 45° oriented mesh within oceanic cells along the border, this would double the kinetic energy and $\partial_t h$ in equations (1b) and (1a) respectively, while the vertical scale factor h and the Coriolis term at the outgoing vorticity points would be mirrored with respect to the cell diagonals. However, our implementation of these conditions did not bring noticeable changes on the 45°-turned solution (not shown), which is already very close to the reference. This result indicates that the sensitivity of circulation within this configuration is controlled primarily by the formulation of advective and diffusive terms, in accord with Dupont et al. (2003).

Motivated by the sensitivity of solutions to the discrete formulation of advection, we investigated the impacts of mesh orientation and coastline indentation using a different advection scheme (EEN). Results are shown in Figure 12 under the free-slip boundary condition. The mesh is progressively turned from left to right (0°, 10°, 30° and 45°) and spatial resolution increases from 1/4° to 1/8°. First, we find that the aligned and intermediate solutions are physically converged at 1/8° resolution (1/16° not shown), contrary to solutions that resorted to ENS or ENE. Second, all solutions are very similar across mesh orientations, even at 1/4° resolution, with a recirculation cell that extends halfway through the basin. These results are quantified in Figure 4 which shows that EEN-based solutions (in solid lines) are virtually identical as early as 1/8°, and that they converge together to the same state as ENS-based solutions as resolution increases to 1/48°.

Vorticity schemes previously used in this study have a 7-point wide stencil, whereas the EEN scheme has a 17-point wide stencil (see Fig. B1). We infer that the larger stencil of the EEN scheme effectively smoothens the discontinuity of the coast, making dynamics much less sensitive to the misalignment of the grid with the physical shorelines. These results advocate for the use of schemes having relatively wide stencils, possibly high-order schemes, to minimise spurious effects of staircase-like coastlines.

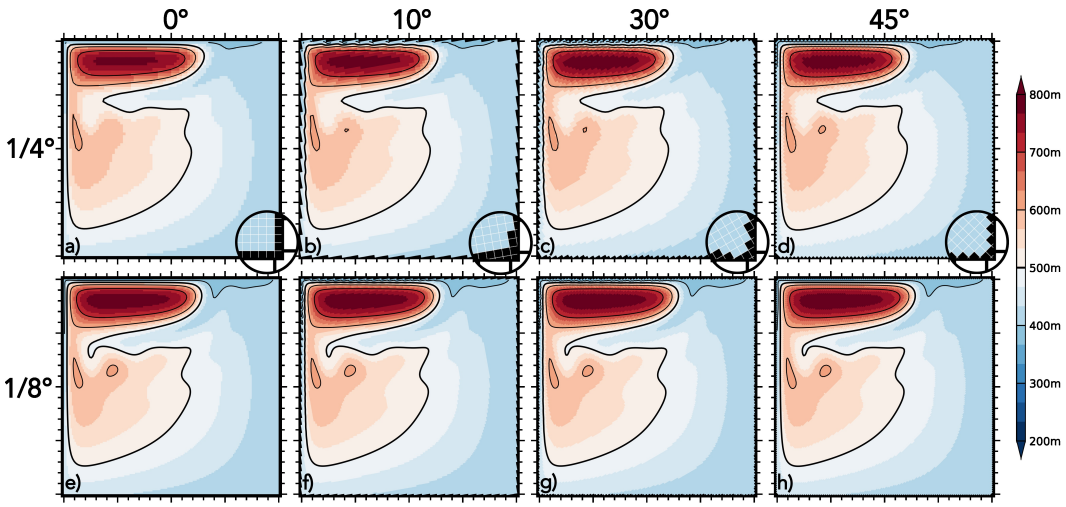

Figure 12. Free-slip solutions solved in vector-invariant form with the EEN advection scheme and the rot-div stress tensor. Shading and isolines (in black) depict the active layer thickness h (isoline 500 m is thickened). x and y main ticks are 500 km apart. From left to right, the mesh is progressively rotated, at 0°, 10°, 30° and 45° with respect to the physical coastline. Spatial resolution increases from 1/4° (top) to 1/8° (bottom).

5 From straight to swerving coastlines

5.1 Dynamics along a cornered coastline

In the previous sections, we explored ways to eliminate spurious effects of artificial steps in model coastlines. However, coastal steps are not always artificial and their effects not necessarily spurious, since real coastlines contain sharp turns that exceed the grid scale and impact boundary currents. For example, a protruding corner in the coastline can cause boundary currents to retroflect (Dupont & Straub, 2004; Deremble et al., 2016), impacting the larger scale circulation (Weeks et al., 2010; Ansorge & Lutjeharms, 2005). Which boundary conditions are most appropriate to model this physical response to a coastal step?

To address this question, we reproduce the configuration of Deremble et al. (2016). The domain is a square basin of 500 km in length, cropped by a 100 km $\times$ 250 km land mass at the southwest end, as illustrated by the grey shading in Figure 13. The equations solved are those given in section 2.1, except that the model is barotropic and excludes wind forcing, bottom friction and the Coriolis effect (parameters are given in Appendix A). The simulation starts with a vortex of negative relative vorticity, standing near the eastern side of the land mass (Fig. 13a). The vortex is then advected up to the corner due to non-linear interaction with the straight coastline. When the vortex begins to overtake the corner, filaments of positive vorticity are generated at the tip, forcing the retroflection of the flow as explained by Deremble et al. (2016). Figure 13b shows the vortex detaching from the coast along a filament of opposite relative vorticity that stretches northeastward from the tip.

5.2 Lateral boundary conditions

On a large-scale isolated step, the definitions of the boundary conditions given in section 2.3 are less straightforward as it is no longer possible to define the local vectors $(\mathbf{n}, \mathbf{t})$ at the singularity. A no-slip condition ($\mathbf{u} = 0$) could potentially hold by continuous extension from the adjacent walls to the tip. However, the definition of the free-slip viscous boundary condition becomes unclear as the normal derivative of the flow is unknown at the tip. Furthermore, by bending a regular coastline toward the limiting case of a protruding corner (κ tends to infinity), the vorticity in equation (5) becomes infinite, suggesting that a singularity in the coastline acts as a source of vorticity in the flow (Deremble et al., 2016).

The detachment or retroflection of the vortex described by Deremble et al. (2016) is driven by advection. We show that this retroflection requires only impermeability conditions along both sides of the land mass and is faithfully represented when viscosity ν is set to zero at the F-node of the singularity (Fig. 13b,e,h). The numerical schemes used in vector-invariant form allow the possibility to enforce $\zeta = 0$ at the tip, causing the retroflection to be no longer simulated (Fig. 13c). If instead a no-slip viscous boundary condition is applied at the tip, vorticity filaments change intensity but are still represented (compare Fig. 13d with Fig. 13b,e,h). While the flux-form equations (whose solution is shown in Fig. 13b) disallow viscous boundary conditions, solutions using the vector-invariant form of equations are thus sensitive to the chosen viscous conditions (Fig. 13c,d,e,h).

When neutralizing the retroflection effect in the advection term (by imposing $\zeta = 0$ at the tip in the advective trends), it is still possible to recover the filament generation and induce retroflection by applying either the no-slip viscous boundary condition (Fig. 13f) or the impermeability condition (not shown) in the diffusive term. However the filament of positive relative vorticity is different in shape and intensity (compare Fig. 13f with Fig. 13b,e,h), its characteristics become more sensitive to the chosen value of viscosity ν (not shown), and its physical interpretation as the detachment of the viscous boundary layer (Deremble et al., 2016) is less straightforward.

The rot-div stress tensor is used for diffusion in the solutions discussed above (Fig. 13b-f,h). In Fig. 13g, we show a solution that uses the symmetric stress tensor combined with the viscosity ν set to zero at the outgoing corner. The solution is quite similar to that obtained using the no-slip condition in the rot-div stress tensor (Fig. 13f). This result concurs with those of section 4 and emphasizes the problematic behaviour of the traditional implementation of slipperiness in the symmetric tensor. These findings also explain why Dupont and Straub (2004) and Deremble et al. (2016) obtained unexpected behaviours at coastal tips when using the combination of symmetric tensor and free-slip viscous boundary condition.

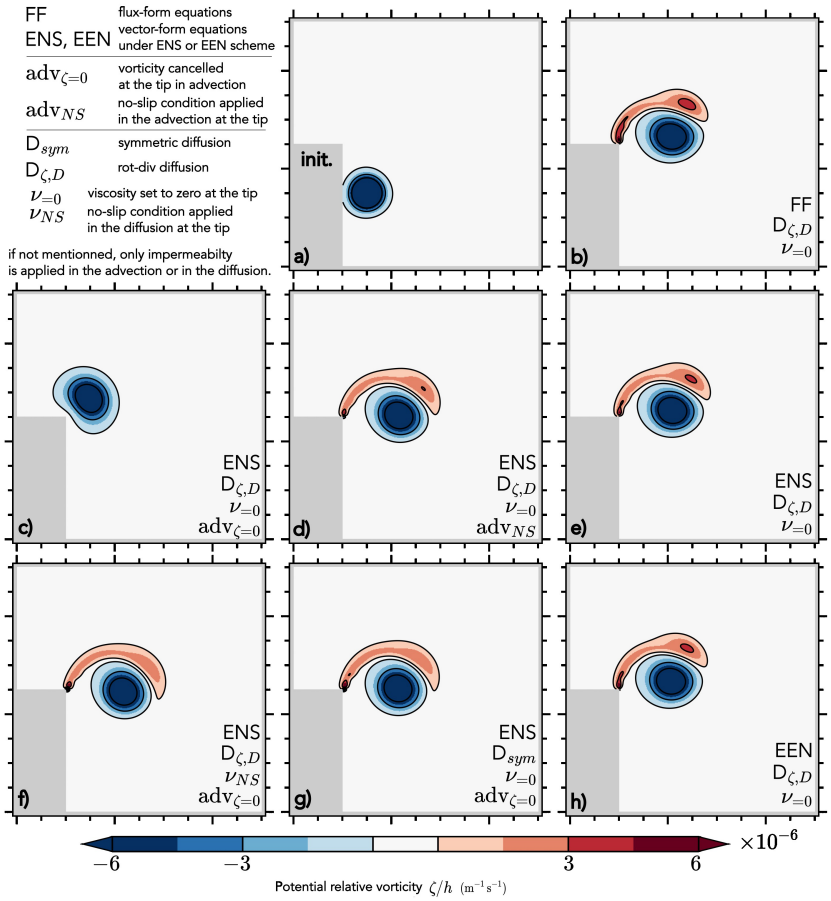

Figure 13. Potential relative vorticity field illustrating the interaction between a cyclonic vortex and a cornered coastline. Panel (a) shows the initial state, (b-h) are snapshots of the potential relative vorticity field after 45 days. Isolines are equivalent to streamlines in this configuration. On all walls, the free-slip boundary condition is applied in advection (vector-invariant form equations only) and in diffusion on both sides of the land mass—except at the tip where different treatments are assessed. Each of these treatments is specified in the bottom right corner of each panel, following notations defined at the top left of the figure.

5.3 Implications for staircase-like coastlines

Staircase-like coastlines studied in sections 3 and 4 using the AM98 configuration can be viewed as a series of small isolated steps. Each step may be expected to have a dynamical effect on the local circulation as described in 5.2, and the ensemble of steps may have a cumulative impact on the basin-scale gyres. For example, the behaviour of solutions using only the impermeability condition, as it is the case in flux-form equations on the 45°-rotated mesh (Fig. 9b,e), can be understood by noting that each step works to retroflect the boundary flow and ultimately distort the gyre circulation. Indeed, in these simulations the viscous boundary condition is free-slip and is applied only in the diffusive term. Therefore, the lack of a zonally extended inertial recirculation (Fig. 9b,e) likely stems from the retroflection — induced by the advection term — of the boundary current on the indented coastline. Interestingly, increasing spatial resolution (while keeping viscosity ν and friction r unchanged) allows the inertial recirculation gyre to grow eastward (compare Fig. 9e with Fig. 9b). An additional simulation (not shown) at a finer resolution of 1/32° confirms this tendency: the inertial recirculation cell then occupies over half of the basin. We interpret this behaviour as the consequence of the reduction of the scale of steps (1/32°) relative to the width of the boundary currents ($\sim$ 1/4°): the production of vorticity filaments, which feeds upon the discontinuity in the flow field across the tips of steps (Deremble et al., 2016), is damped if steps are too small to generate sizeable discontinuities.

6 Conclusions

We revisited the 'staircase problem' highlighted by AM98, who exposed the existence of a spurious form drag when smooth coastlines are numerically transformed into steps. We reproduced their configuration, which consists of a square closed basin under shallow water dynamics and cyclonic wind forcing, simulated on a Cartesian mesh with varying orientation. We tested various mesh resolutions with many combinations of advection formulations (flux or vector-invariant forms of equations with potential-enstrophy (ENS), energy (ENE) or energy and potential-enstrophy (EEN) conserving schemes developed by Sadourny) and two commonly used viscous stress tensors (rot-div and symmetric formulations).

We first show that the free-slip non-rotated solution is not physically converged at 1/4° resolution, under ENS or ENE, but only from 1/16° with the same viscosity and friction parameters as AM98. By *physical convergence* we mean the insensitivity of the main characteristics of the flow to further increase of the mesh resolution. Such convergence requires to resolve the inertial dynamics induced by the free-slip (i.e. mirror) boundary condition along the northern coast by having at least four grid points per internal radius of deformation, which is close to 30 km in this region.

In addition, we find that the 45°-rotated free-slip solution is also physically converged from 1/16° resolution and surprisingly looks almost identical to the aligned 1/16° solution, contrary to AM98. The reason is that the free-slip boundary condition (zero vorticity) applied at the tips of coastal indents created by the 45°-rotated mesh exactly stands for a straight shoreline passing through T and F nodes of a C-grid. At intermediate angles of mesh orientation (strictly between 0° and 45°), physically converged solutions are only achieved near 1/32° resolution and depart from the non- or 45°-rotated 1/16° solution. We suggest that the different sensitivity and delayed convergence at intermediate angles stem from inaccurate declaration of the free-slip boundary condition as the resulting numerical frontier is corrugated, not straight.

The above-mentioned results hold in vector-invariant form with the ENS or ENE scheme combined with the rot-div stress tensor. When switching to the symmetric stress tensor or to flux-form advection, rotated solutions no longer converge toward the reference (aligned) solution and instead resemble no-slip solutions. In both cases, applying a *true* mirror boundary condition with respect to the physical coastline on the 45°-rotated mesh allows to retrieve solutions close to the reference at 1/16° resolution. These results pinpoint the spurious behaviour of the traditional implementation of 'free-slip' in the symmetric viscous tensor, which works as intended only if the mesh is aligned with the border.

Importantly, using an advection scheme with a larger stencil (EEN in vector-invariant form) makes the free-slip solutions virtually identical from 1/8° for any orientation of the mesh. We infer that larger stencils allow advection schemes and the simulated circulation to become much less sensitive to broken coastlines, providing a practical avenue to mitigate spurious effects of piecewise-constant land-ocean frontiers.

In addition to exposing ways to eliminate spurious effects of artificial coastal steps, we explored the numerical treatment of a single sharp turn in the physical coastline, using the configuration of Deremble et al. (2016). One expected impact of a large protruding corner in the coastline is the generation of vorticity filaments that force the boundary current to retroflect (Deremble et al., 2016). We show that the correct way to represent this phenomenon is to apply only an impermeability condition in advection at the maxima of curvature. Using a viscous boundary condition in the advection scheme may either cancel (free-slip) or alter (no-slip) the phenomenon.

We conclude that staircase-like coastlines can behave like straight and slippery coastlines provided that coastal dynamics are physically resolved and that an accurate mir-

Table A1. Grid-size and time-step used in discretisation for AM98's configuration

Resolution	1/4°	1/8°	1/16°	1/32°	1/48°
Grid-spacing	25 km	12.5 km	6.25 km	3.125 km	$\sim$ 2.1 km
Time-step	30 min	15 min	7.5 min	3 min	1.5 min

ror boundary condition is used. To minimise spurious effects of artificial steps in OGCM boundaries, we recommend the use of advection schemes with large stencils (such as the energy-enstrophy conserving (EEN) scheme), combined with free-slip (zero vorticity) boundary conditions and the rot-div viscous stress tensor. If flux-form equations or the symmetric stress tensor are chosen, free-slip along staircase-like coastlines is best implemented with general techniques such as immersed boundary methods. However, perfect slipperiness may not be desirable to represent the impact on boundary currents of sharp turns in the real coastline; in this case, exclusive application of impermeability conditions may better represent physical flow-topography interactions than a free-slip boundary condition.

Appendix A Numerical parameters

In the AM98 configuration, the initial state is at rest with the thickness of the active layer uniformly equal to $h_0 = 500\,\mathrm{m}$. Density is $\rho_0 = 1000\,\mathrm{kg\,m^{-3}}$ and reduced gravity $g' = 0.02\,\mathrm{N\,s^{-2}}$. The Coriolis parameter evolves on a beta-plane $f(y) = f_0 + \beta y$ where $f_0 = 0.5\ 10^{-4}\,\mathrm{s^{-1}}$ and $\beta = 2 \times 10^{-11}\,\mathrm{m\,s^{-1}}$ so that the internal radius of deformation $R = \sqrt{g'h_0}/f$ is about 45 km at the mid-basin. Zonal wind stress is $\tau = -\tau_0 \cos(\pi y/L)$ with $\tau_0 = 0.2\,\mathrm{Nm^{-2}}$. Uniform friction parameters are considered with $r = 10^{-7}\,\mathrm{s^{-1}}$ the bottom linear friction and $\nu = 500\,\mathrm{m^2\,s^{-1}}$ the lateral viscosity. Uniform mesh resolution ($\Delta x = \Delta y$) and associated time-step for the AM98 configuration are summarised in Table A1. The Asselin filter parameter of the Leap Frog Robert-Asselin time-stepping scheme is $\epsilon = 10^{-1}$. In vector-form, gradient of kinetic energy is discretised with a second order centered scheme. In flux form, advection is also discretised with a second order centered scheme while the Coriolis term is discretised with the ENS scheme.

In the single vortex configuration of Deremble et al. (2016), the initial condition is a vortex of negative vorticity placed next to the wall. In the relative frame of reference centered on the vortex, the initial horizontal speeds are given by the azimuthal profile v_θ (Lamb-Oseen vortex):

$$v_\theta = \frac{\Gamma}{2\pi r}\left(1 - \exp\left(-\frac{r^2}{2r_0^2}\right)\right) \tag{A1}$$

with the pseudoradius $r_0 = 20\,\mathrm{km}$ and the strength of the vortex $\Gamma = -5 \times 10^4\,\mathrm{m^2\,s^{-1}}$. The basin depth h is 1 m deep. Lateral viscosity is $\nu = 20\ \mathrm{m^2\ s^{-1}}$. Simulations are ran over 45 days with an uniform spatial resolution of $\Delta x = \Delta y = 1.25\,\mathrm{km}$ and a time-step of 90 s.

Appendix B Formulation of the discrete vorticity schemes used in vector-invariant form simulations

The discrete vorticity schemes considered in this study are defined on the Arakawa C-grid. The grid is staggered so that total vorticity $\zeta_{i,j}+f_{i,j}$, horizontal velocities $(u_{i,j}; v_{i,j})$ and height $h_{i,j}$ variables are arranged as shown in Figure B1a. The total potential vorticity $q = \frac{(\zeta+f)}{h_f}$ is needed for vector-invariant form advection so layer thickness at F-

nodes h_f is deduced from the height h nodes: $h_f = \overline{\overline{h}}^{i,j}$; while vorticity is diagnosed as follows:

$$\zeta_{i,j} = \frac{1}{e_1 e_{2f}} \left(\delta_i \left[e_{2v} v \right] - \delta_j \left[e_{1u} u \right] \right) \tag{B1}$$

where $(\overline{\ }^i, \overline{\ }^j)$ and (δ_i, δ_j) are the averaging and differencing operators at the mid point, e.g., $\overline{h}^i = \frac{1}{2}(h_{i,j} + h_{i+1,j})$ and $\delta_i v = v_{i+1,j} - v_{i,j}$. The horizontal scale factors e_{1t}, e_{1u}, e_{1v} and e_{1f} (e_{2t}, e_{2u}, e_{2v} and e_{2f}) are derived analytically at each node from the latitudinal (longitudinal) coordinate; on a uniform regular mesh, they are all equal to $\Delta x = \Delta y$.

Figure B1b-d represents the discretisation at $u_{i,j}$ nodes (blue disks) and illustrates the size of the stencil for each scheme. First, the potential enstrophy conserving scheme (Fig. B1b) (Sadourny, 1975) provides a global conservation of global enstrophy $h_f q^2$ for non-divergent flow. For x and y components of the vorticity term, it writes as:

$$+\frac{1}{e_{1u}} \overline{q}^j \overline{\overline{V}}^{i,j} \tag{B2}$$

$$-\frac{1}{e_{2v}} \overline{q}^i \overline{\overline{U}}^{i,j} \tag{B3}$$

where $(U; V)$ are the transports across cell faces, e.g., $V = e_{1v} h_v v$. Then, the kinetic energy conserving (ENE) vorticity scheme (Fig. B1c) (Sadourny, 1975) is defined as:

$$+\frac{1}{e_{1u}} \overline{q \overline{V}^i}^j \tag{B4}$$

$$-\frac{1}{e_{2v}} \overline{q \overline{U}^j}^i \tag{B5}$$

Finally, the EEN scheme developed by Sadourny (Burridge & Haseler, 1977) is a member of the family of vorticity schemes derived by Arakawa and Lamb (1981) that conserves kinetic energy and, provided there is no divergence in the flow, potential enstrophy. This scheme relies upon averaging triads of vorticity ${}^i_j\mathrm{Q}^l_m$ that ultimately widen the stencil up to 17 velocity nodes; instead of 7 in the ENS or ENE schemes as they use a much cheaper two-point averaging. A triad ${}^i_j\mathrm{Q}^l_m$ is defined as:

$${}^i_j\mathrm{Q}^l_m = \frac{1}{12} \left(q^{i-1/2-l}_{j-1/2+m} + q^{i-1/2+m}_{j-1/2+l} + q^{i-1/2+l}_{j-1/2-m} \right) \tag{B6}$$

with $(l, m) \in I^2$ where $I = (1/2\,;\, -1/2)$. Each triad combines with the adjacent transport V^i_j, e.g., V^{i+1}_j multiplies with ${}^{i+1}_j\mathrm{Q}^{-1/2}_{1/2}$ (in red in Fig. B1d). Expressions for EEN scheme summarize as

$$+\frac{1}{e_{1u}} \sum\nolimits_{l,m \in I^2} {}^{i+1/2-l}_{\ \ j}\mathrm{Q}^l_m \; V^{i+1/2-l}_{j-1/2+m} \tag{B7}$$

$$-\frac{1}{e_{2v}} \sum\nolimits_{l,m \in I^2} {}^{\ \ i}_{j+1/2-m}\mathrm{Q}^l_m \; U^{i-1/2+l}_{j+1/2-m} \tag{B8}$$

Availability Statement

NEMO code is available at `https://forge.nemo-ocean.eu/nemo/nemo`. The described version is 4.2. The configurations are available at https://doi.org/10.5281/zenodo.7480139 and the plotting scripts are available at https://doi.org/10.5281/zenodo.7480159.

Acknowledgments

We sincerely thank Sibylle Techene for her support and performing RK3 simulations. This work was granted access to the HPC resources of IDRIS under the allocation 2021-A0100107451 made by GENCI.

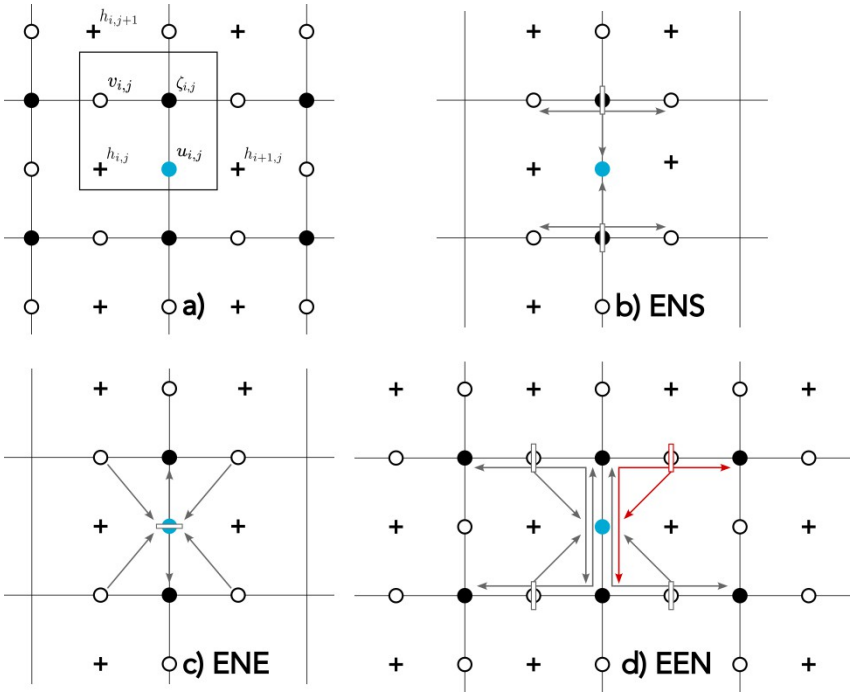

Figure B1. Discrete vorticity schemes on the Arakawa C-grid. (a) Location and indexing of height h nodes (black crosses), horizontal velocity u and v nodes (black circles) and vorticity ζ nodes (black disks) on a single cell. Panels (b), (c) and (d) illustrate respectively the ENS, ENE and EEN discretisation of vorticity in vector-invariant form. Single arrows (in grey) add themselves; double arrows represent two-point averaging; right-angle cornered arrows symbolize triads ${}^{i}_{j}\mathrm{Q}^{l}_{m}$; and rectangles (grey edged) is the factoring of the averaged quantities with the local variables.

References

Adcroft, A., & Marshall, D. (1998, January). How slippery are piecewise-constant coastlines in numerical ocean models? *Tellus A: Dynamic Meteorology and Oceanography*, *50*(1), 95–108. Retrieved 2020-02-19, from https://doi.org/10.3402/tellusa.v50i1.14514 doi: 10.3402/tellusa.v50i1.14514

Ansorge, I. J., & Lutjeharms, J. R. E. (2005). Direct observations of eddy turbulence at a ridge in the Southern Ocean. *Geophysical Research Letters*, *32*(14). Retrieved 2022-02-18, from https://onlinelibrary.wiley.com/doi/abs/10.1029/2005GL022588 (_eprint: https://onlinelibrary.wiley.com/doi/pdf/10.1029/2005GL022588) doi: 10.1029/2005GL022588

Arakawa, A., & Lamb, V. R. (1981, January). A Potential Enstrophy and Energy Conserving Scheme for the Shallow Water Equations. *Monthly Weather Review*, *109*(1), 18–36. Retrieved 2022-01-24, from https://journals.ametsoc.org/view/journals/mwre/109/1/1520-0493_1981_109_0018_apeaec_2_0_co_2.xml (Publisher: American Meteorological Society Section: Monthly Weather Review) doi: 10.1175/1520-0493(1981)109⟨0018:APEAEC⟩2.0.CO;2

Bleck, R., & Boudra, D. (1986). Wind-driven spin-up in eddy-resolving ocean models formulated in isopycnic and isobaric coordinates. *Journal of Geophysical Research: Oceans*, *91*(C6), 7611–7621. Retrieved 2022-10-24, from https://onlinelibrary.wiley.com/doi/abs/10.1029/JC091iC06p07611 (_eprint: https://onlinelibrary.wiley.com/doi/pdf/10.1029/JC091iC06p07611) doi: 10.1029/JC091iC06p07611

Burridge, D., & Haseler, J. (1977). A model for medium range weather forecasting. *Tech. Rep. No.4,ECMWF*.

Causon, D. M., Ingram, D. M., Mingham, C. G., Yang, G., & Pearson, R. V. (2000, February). Calculation of shallow water flows using a Cartesian cut cell approach. *Advances in Water Resources*, *23*(5), 545–562. Retrieved 2022-05-03, from https://www.sciencedirect.com/science/article/pii/S0309170899000366 doi: 10.1016/S0309-1708(99)00036-6

Cessi, P. (1991, November). Laminar separation of colliding western boundary currents. *Journal of Marine Research*, *49*(4), 697–717. doi: 10.1357/002224091784995738

Deremble, B., Dewar, W. K., & Chassignet, E. P. (2016, November). Vorticity dynamics near sharp topographic features. *Journal of Marine Research*, *74*(6), 249–276. doi: 10.1357/002224016821744142

Dupont, F., & Straub, D. N. (2004, January). Effect of a wavy wall on the single gyre Munk problem. *Tellus A: Dynamic Meteorology and Oceanography*, *56*(4), 387–399. Retrieved 2021-09-16, from https://www.tandfonline.com/doi/full/10.3402/tellusa.v56i4.14422 doi: 10.3402/tellusa.v56i4.14422

Dupont, F., Straub, D. N., & Lin, C. A. (2003, January). Influence of a step-like coastline on the basin scale vorticity budget of mid-latitude gyre models. *Tellus A: Dynamic Meteorology and Oceanography*, *55*(3), 255–272. Retrieved 2020-02-20, from https://doi.org/10.3402/tellusa.v55i3.12094 doi: 10.3402/tellusa.v55i3.12094

Ezer, T. (2016, August). Revisiting the problem of the Gulf Stream separation: on the representation of topography in ocean models with different types of vertical grids. *Ocean Modelling*, *104*, 15–27. Retrieved 2022-10-11, from https://linkinghub.elsevier.com/retrieve/pii/S1463500316300397 doi: 10.1016/j.ocemod.2016.05.008

Gent, P. R. (1993, May). The Energetically Consistent Shallow-Water Equations. *Journal of the Atmospheric Sciences*, *50*(9), 1323–1325. Retrieved 2022-11-21, from https://journals.ametsoc.org/view/journals/atsc/50/9/1520-0469_1993_050_1323_tecswe_2_0_co_2.xml (Publisher: American Meteorological Society Section: Journal of the Atmospheric Sciences) doi:

10.1175/1520-0469(1993)050⟨1323:TECSWE⟩2.0.CO;2

Griffies, S. M., & Hallberg, R. W. (2000). Biharmonic Friction with a Smagorinsky-Like Viscosity for Use in Large-Scale Eddy-Permitting Ocean Models. *MONTHLY WEATHER REVIEW*, *128*, 12.

Griffiths, S. D. (2013, December). Kelvin wave propagation along straight boundaries in C-grid finite-difference models. *Journal of Computational Physics*, *255*, 639–659. Retrieved 2020-09-21, from https://linkinghub.elsevier.com/retrieve/pii/S0021999113005846 doi: 10.1016/j.jcp.2013.08.040

Hallberg, R. (2013, December). Using a resolution function to regulate parameterizations of oceanic mesoscale eddy effects. *Ocean Modelling*, *72*, 92–103. Retrieved 2020-09-02, from https://linkinghub.elsevier.com/retrieve/pii/S1463500313001601 doi: 10.1016/j.ocemod.2013.08.007

Holland, W. R., & Haidvogel, D. B. (1981, April). On the Vacillation of an Unstable Baroclinic Wave Field in an Eddy-Resolving Model of the Oceanic General Circulation. *Journal of Physical Oceanography*, *11*(4), 557–568. Retrieved 2021-11-16, from https://journals.ametsoc.org/view/journals/phoc/11/4/1520-0485_1981_011_0557_otvoau_2_0_co_2.xml (Publisher: American Meteorological Society Section: Journal of Physical Oceanography) doi: 10.1175/1520-0485(1981)011⟨0557:OTVOAU⟩2.0.CO;2

Ketefian, G. S., & Jacobson, M. Z. (2011, April). A mass, energy, vorticity, and potential enstrophy conserving lateral boundary scheme for the shallow water equations using piecewise linear boundary approximations. *Journal of Computational Physics*, *230*(8), 2751–2793. Retrieved 2022-04-20, from https://www.sciencedirect.com/science/article/pii/S0021999110006108 doi: 10.1016/j.jcp.2010.11.008

Kirkpatrick, M. P., Armfield, S. W., & Kent, J. H. (2003, January). A representation of curved boundaries for the solution of the Navier–Stokes equations on a staggered three-dimensional Cartesian grid. *Journal of Computational Physics*, *184*(1), 1–36. Retrieved 2022-05-03, from https://www.sciencedirect.com/science/article/pii/S002199910200013X doi: 10.1016/S0021-9991(02)00013-X

Leclair, M., & Madec, G. (2009, January). A conservative leapfrog time stepping method. *Ocean Modelling*, *30*(2), 88–94. Retrieved 2021-11-18, from https://www.sciencedirect.com/science/article/pii/S1463500309001206 doi: 10.1016/j.ocemod.2009.06.006

Madec, G., Delecluse, P., Crepon, M., & Chartier, M. (1991, September). A Three-Dimensional Numerical Study of Deep-Water Formation in the Northwestern Mediterranean Sea. *Journal of Physical Oceanography*, *21*(9), 1349–1371. Retrieved 2022-01-25, from https://journals.ametsoc.org/view/journals/phoc/21/9/1520-0485_1991_021_1349_atdnso_2_0_co_2.xml (Publisher: American Meteorological Society Section: Journal of Physical Oceanography) doi: 10.1175/1520-0485(1991)021⟨1349:ATDNSO⟩2.0.CO;2

Madec, G., & NEMO System Team. (2022). NEMO ocean engine. (Publisher: Zenodo) doi: 10.5281/zenodo.6334656

Magaldi, M. G., Özgökmen, T. M., Griffa, A., Chassignet, E. P., Iskandarani, M., & Peters, H. (2008, January). Turbulent flow regimes behind a coastal cape in a stratified and rotating environment. *Ocean Modelling*, *25*(1), 65–82. Retrieved 2022-02-18, from https://www.sciencedirect.com/science/article/pii/S1463500308000887 doi: 10.1016/j.ocemod.2008.06.006

Sadourny, R. (1975, April). The Dynamics of Finite-Difference Models of the Shallow-Water Equations. *Journal of the Atmospheric Sciences*, *32*(4), 680–689. Retrieved 2020-02-27, from https://journals.ametsoc.org/doi/abs/10.1175/1520-0469(1975)032%3C0680:TDOFDM%3E2.0.CO;2 (Publisher: American Meteorological Society) doi: 10.1175/1520-0469(1975)032⟨0680:TDOFDM⟩2.0.CO;2

Shchepetkin, A. F., & O'Brien, J. J. (1996, June). A Physically Consistent Formulation of Lateral Friction in Shallow-Water Equation Ocean Models. *Monthly Weather Review*, *124*(6), 1285–1300. Retrieved 2022-01-10, from https://journals.ametsoc.org/view/journals/mwre/124/6/1520-0493_1996_124_1285_apcfol_2_0_co_2.xml (Publisher: American Meteorological Society Section: Monthly Weather Review) doi: 10.1175/1520-0493(1996)124⟨1285:APCFOL⟩2.0.CO;2

Verron, J., & Blayo, E. (1996, September). The No-Slip Condition and Separation of Western Boundary Currents. *Journal of Physical Oceanography*, *26*(9), 1938–1951. Retrieved 2020-11-23, from https://journals.ametsoc.org/jpo/article/26/9/1938/8943/The-No-Slip-Condition-and-Separation-of-Western (Publisher: American Meteorological Society) doi: 10.1175/1520-0485(1996)026⟨1938:TNSCAS⟩2.0.CO;2

Warner, S. J., & MacCready, P. (2009, November). Dissecting the Pressure Field in Tidal Flow past a Headland: When Is Form Drag "Real"? *Journal of Physical Oceanography*, *39*(11), 2971–2984. Retrieved 2022-02-18, from https://journals.ametsoc.org/view/journals/phoc/39/11/2009jpo4173.1.xml (Publisher: American Meteorological Society Section: Journal of Physical Oceanography) doi: 10.1175/2009JPO4173.1

Weeks, S. J., Bakun, A., Steinberg, C. R., Brinkman, R., & Hoegh-Guldberg, O. (2010, December). The Capricorn Eddy: a prominent driver of the ecology and future of the southern Great Barrier Reef. *Coral Reefs*, *29*(4), 975–985. Retrieved 2022-02-18, from https://doi.org/10.1007/s00338-010-0644-z doi: 10.1007/s00338-010-0644-z

Figure 1.

real coastsline

smoothed coastline

Figure 2.

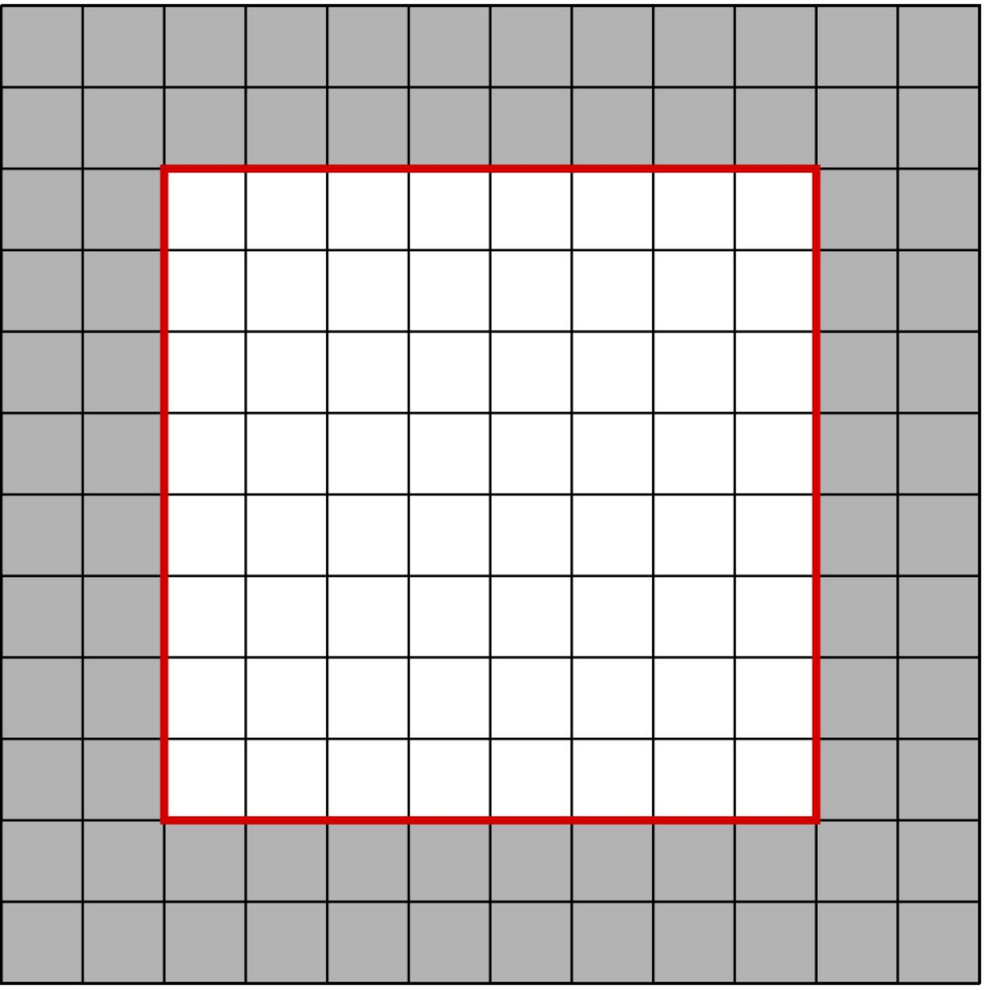

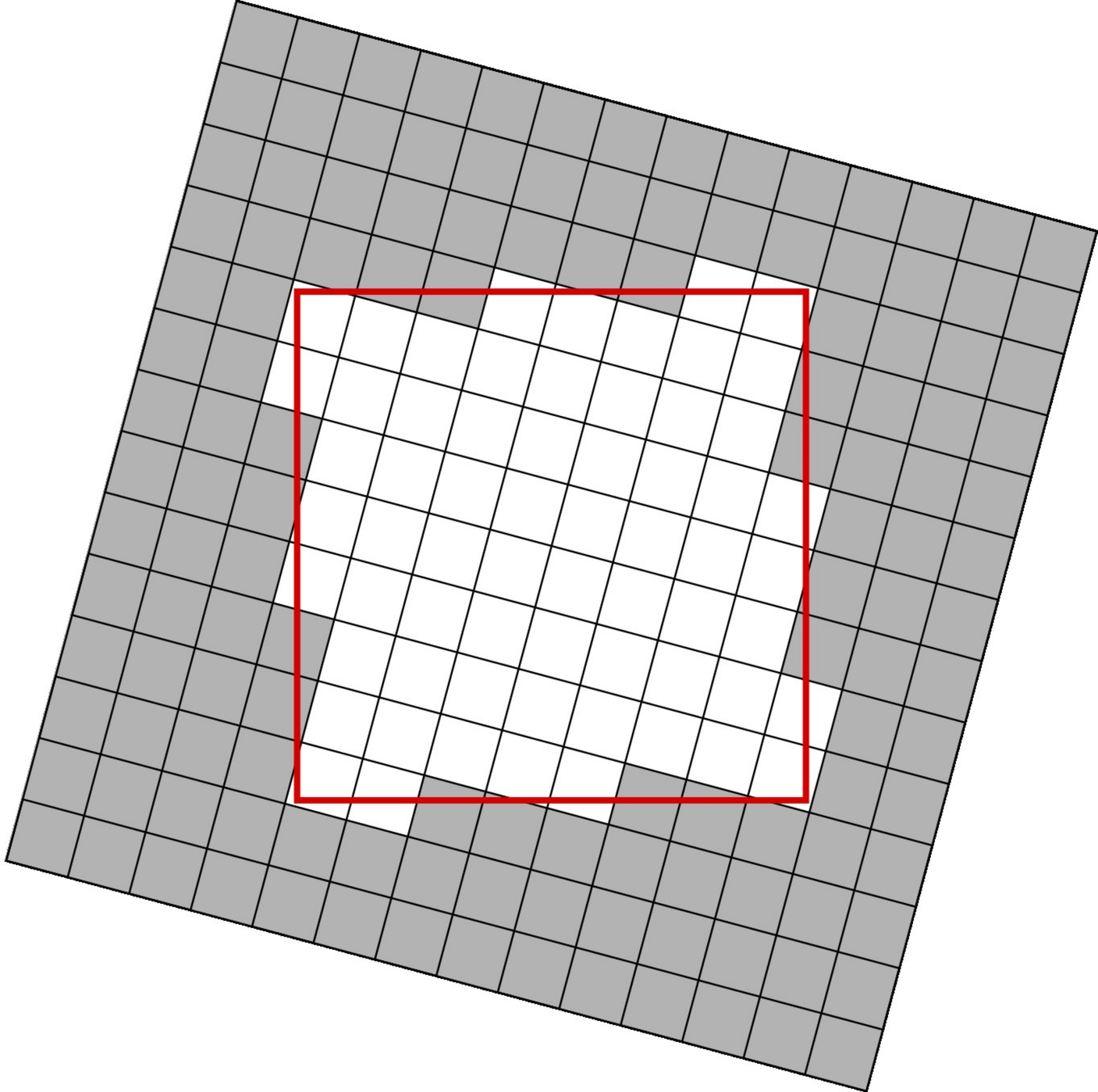

Figure 3.

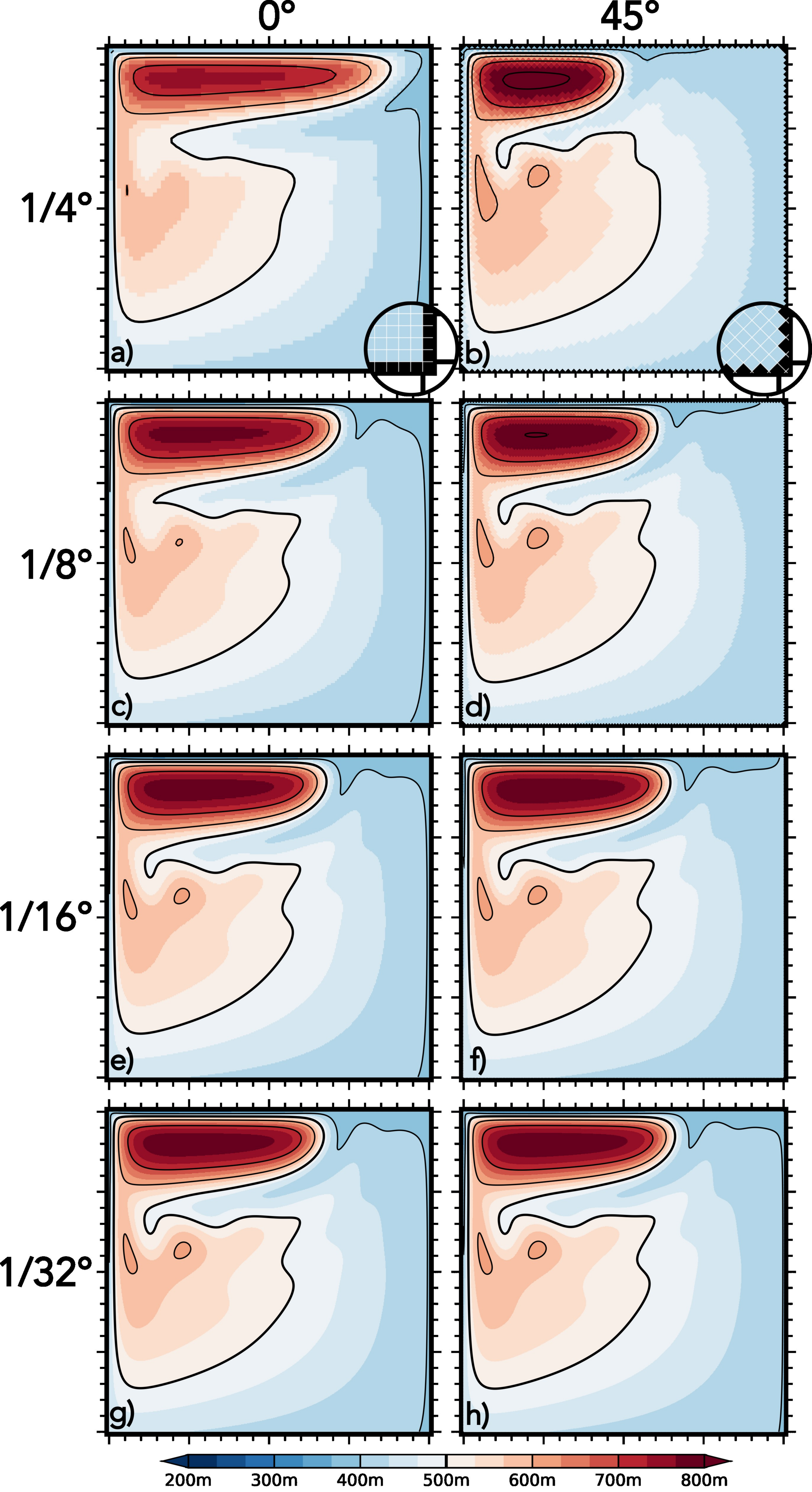
0°
45°
1/4°
1/8°
1/16°
1/32°
a)
b)
c)
d)
e)
f)
g)
h)
200m
300m
400m
500m
600m
700m
800m

Figure 4.

Extension (km)

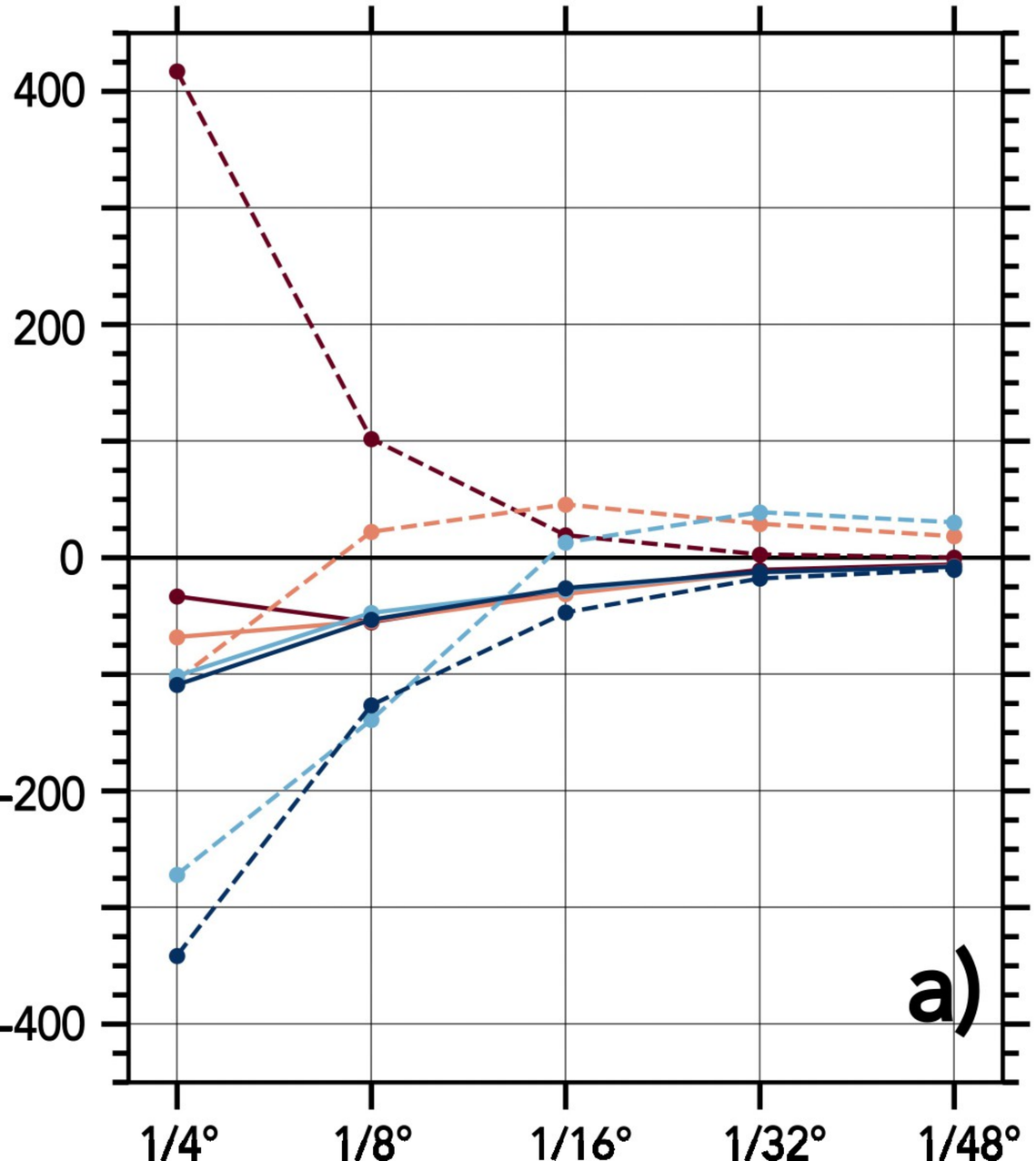

Intensity (m)

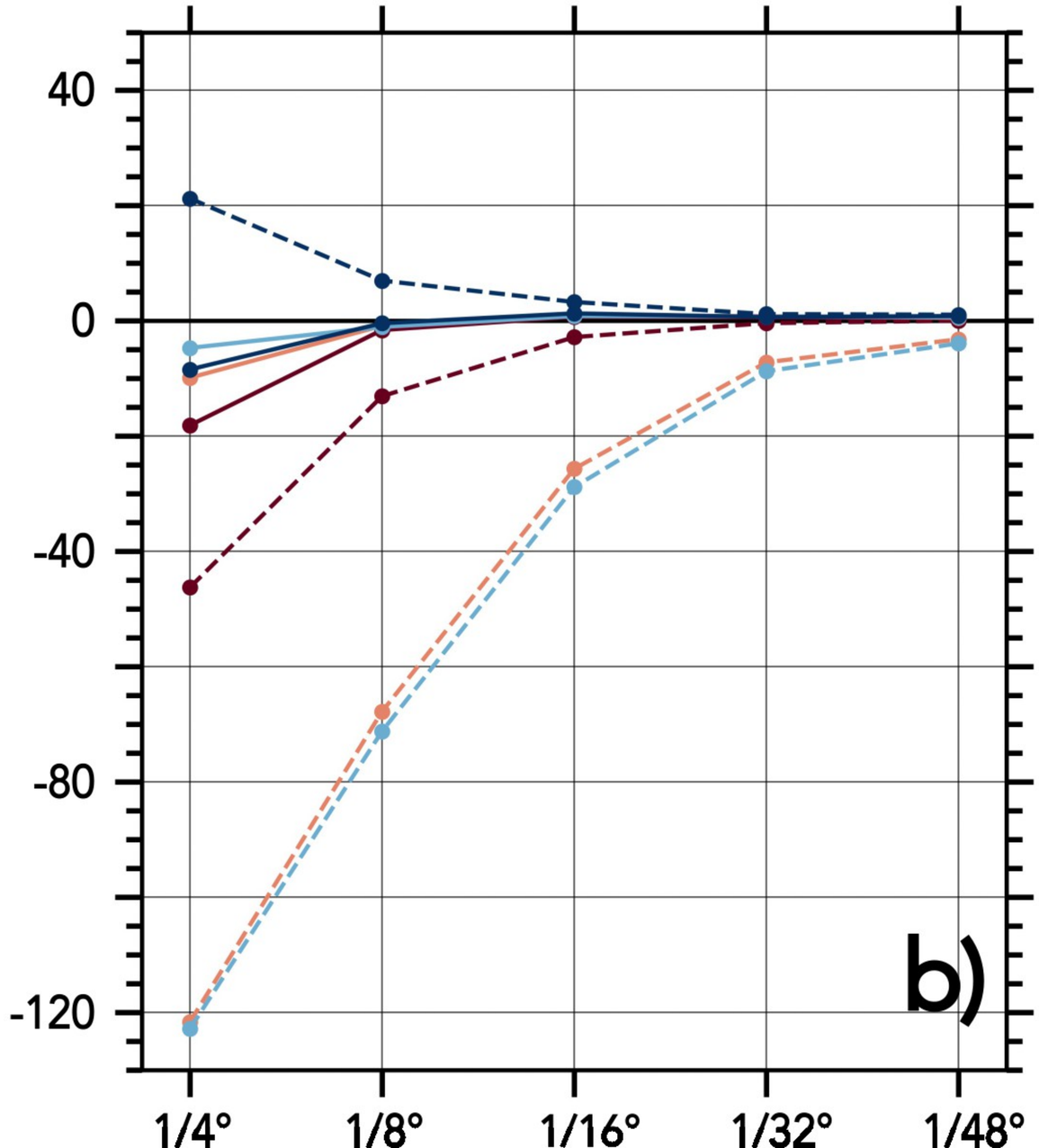

Figure 5.

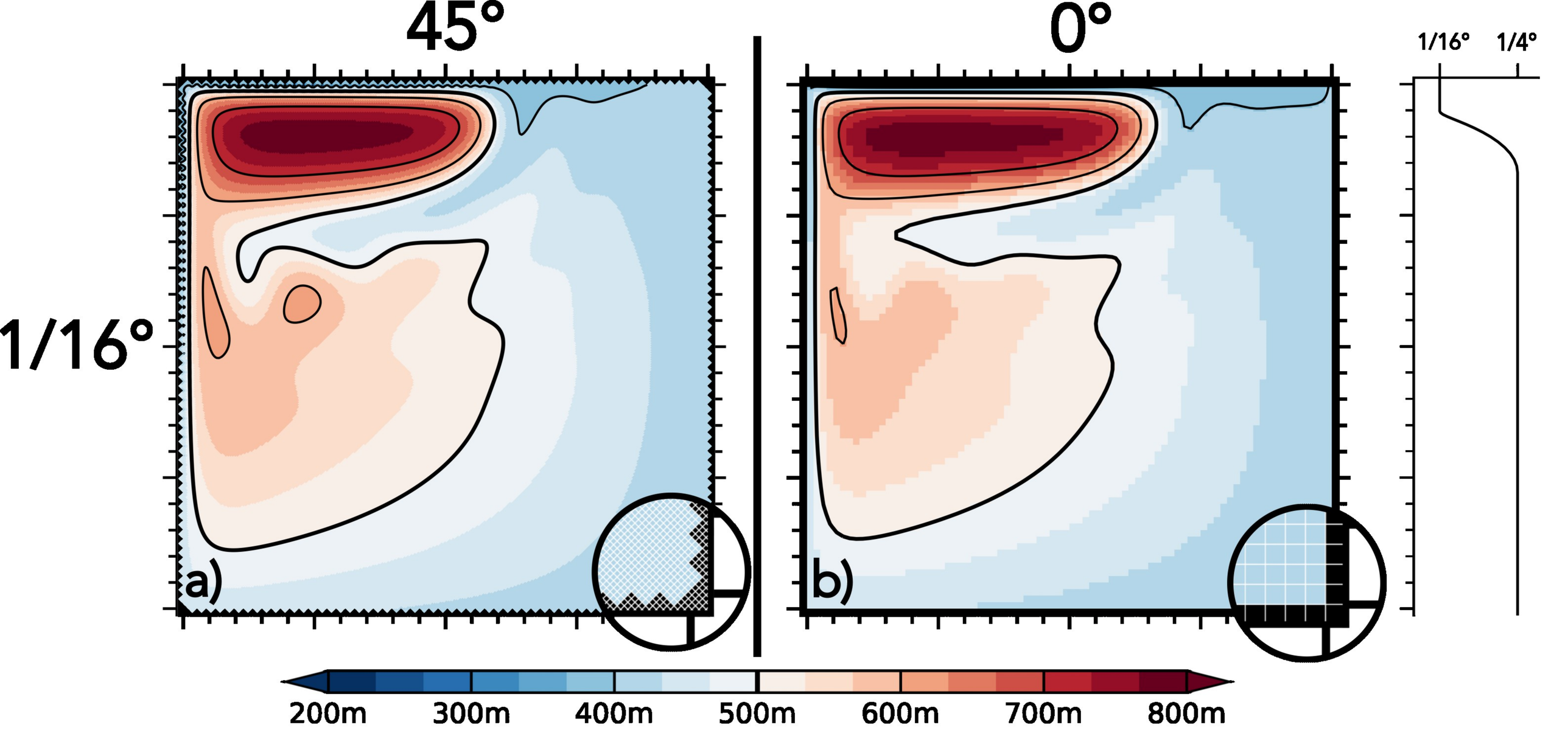
45°
0°
1/16°
1/16°
1/4°
a)
b)
200m
300m
400m
500m
600m
700m
800m

Figure 6.

0°

45°

1/4°

1/16°

a)

b)

c)

d)

800m

700m

600m

500m

400m

300m

200m

Figure 7.

0°

45°

45° + mirror cond.

1/4°

1/16°

a)

b)

c)

d)

e)

f)

800m

700m

600m

500m

400m

300m

200m

Figure 8.

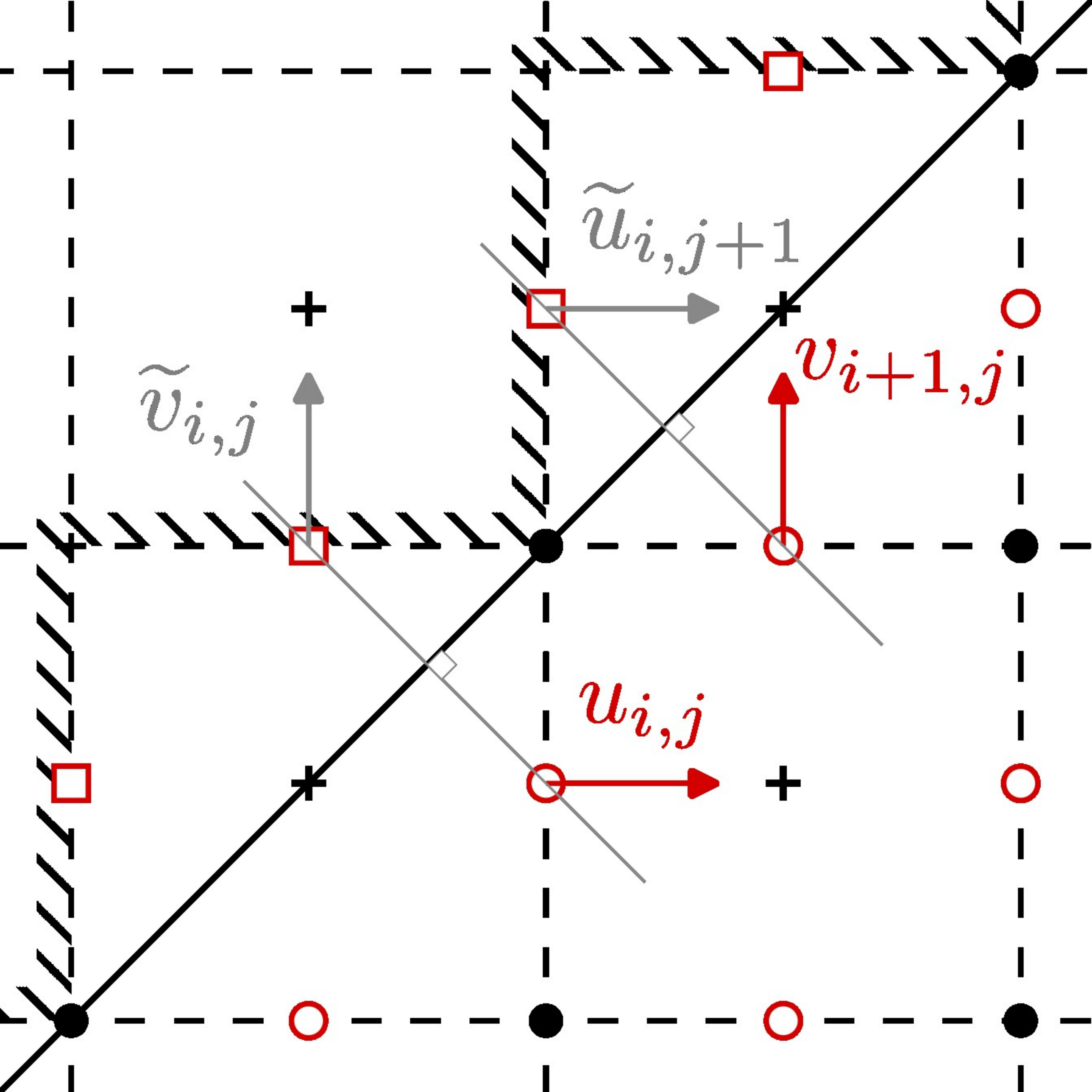
$\widetilde{u}_{i,j+1}$
$\widetilde{v}_{i,j}$
$v_{i+1,j}$
$u_{i,j}$

Figure 9.

0°

45°

45° + mirror cond.

1/4°

1/16°

a)

b)

c)

d)

e)

f)

800m

700m

600m

500m

400m

300m

200m

Figure 10.

10°

30°

1/4°

1/8°

1/16°

1/32°

a)

b)

c)

d)

e)

f)

g)

h)

200m 300m 400m 500m 600m 700m 800m

Figure 11.

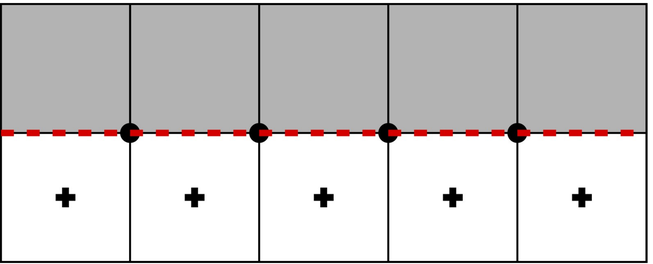

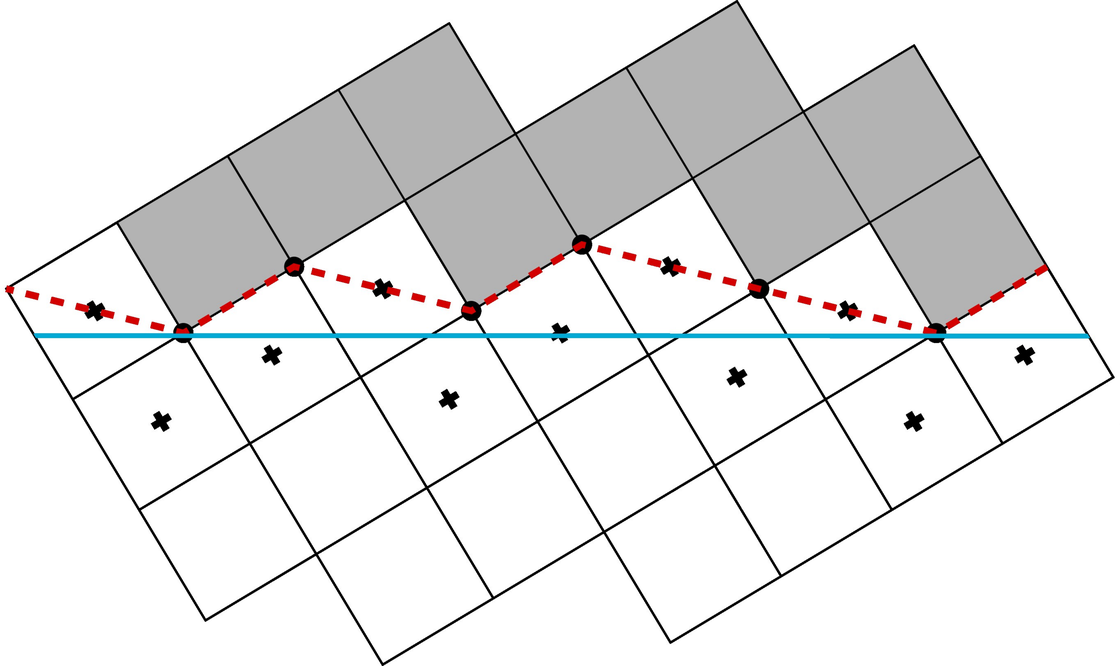

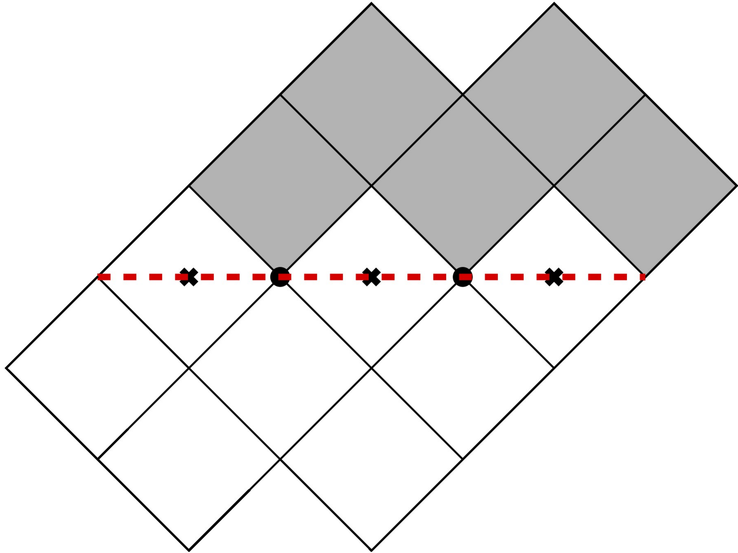

Figure 12.

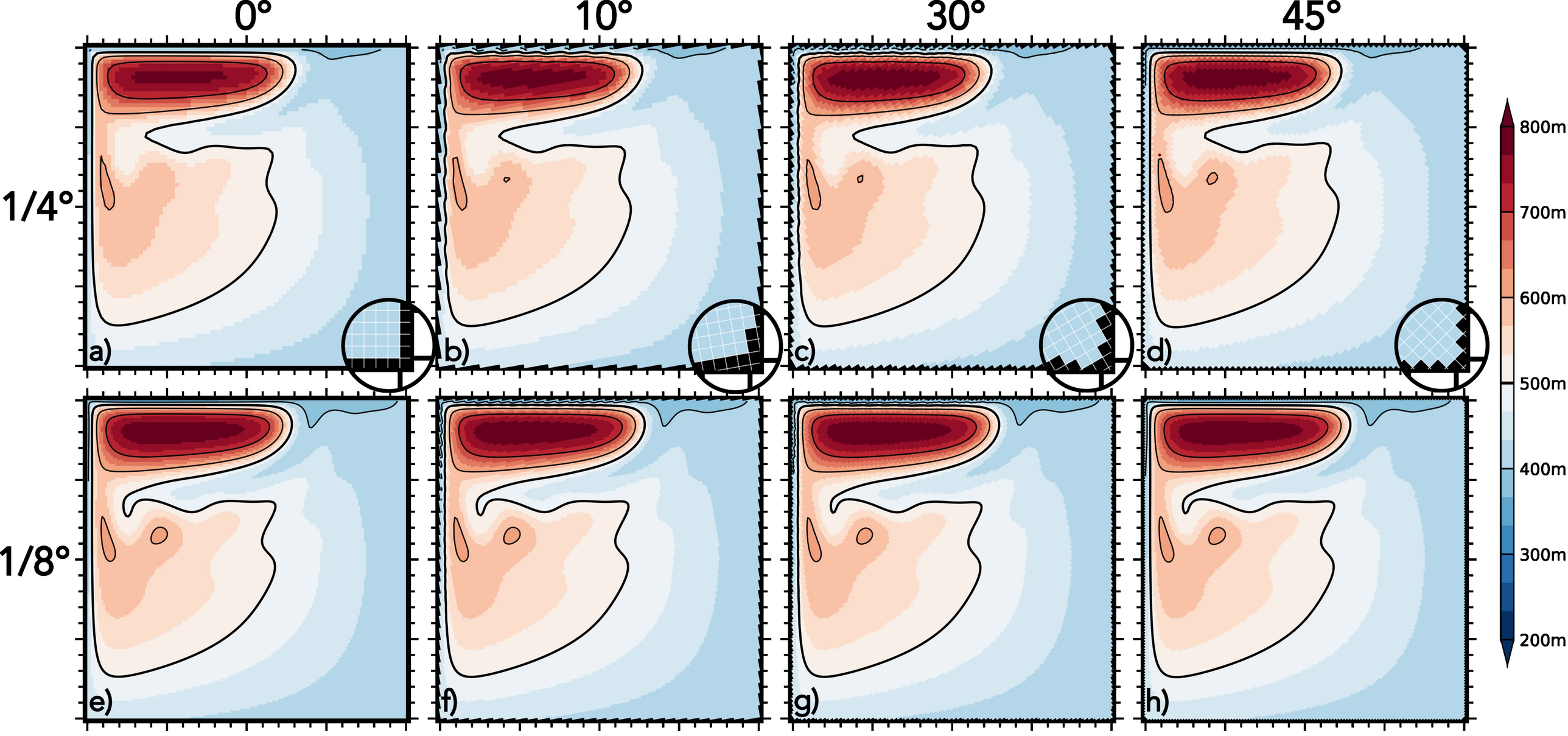
0°
10°
30°
45°
1/4°
1/8°
a)
b)
c)
d)
e)
f)
g)
h)
800m
700m
600m
500m
400m
300m
200m

Figure 13.

FF flux-form equations
ENS, EEN vector-form equations under ENS or EEN scheme

$\mathrm{adv}_{\zeta=0}$ vorticity cancelled at the tip in advection

adv_{NS} no-slip condition applied in the advection at the tip

D_{sym} symmetric diffusion

$\mathrm{D}_{\zeta,D}$ rot-div diffusion

$\nu_{=0}$ viscosity set to zero at the tip

ν_{NS} no-slip condition applied in the diffusion at the tip

if not mentionned, only impermeabilty is applied in the advection or in the diffusion.

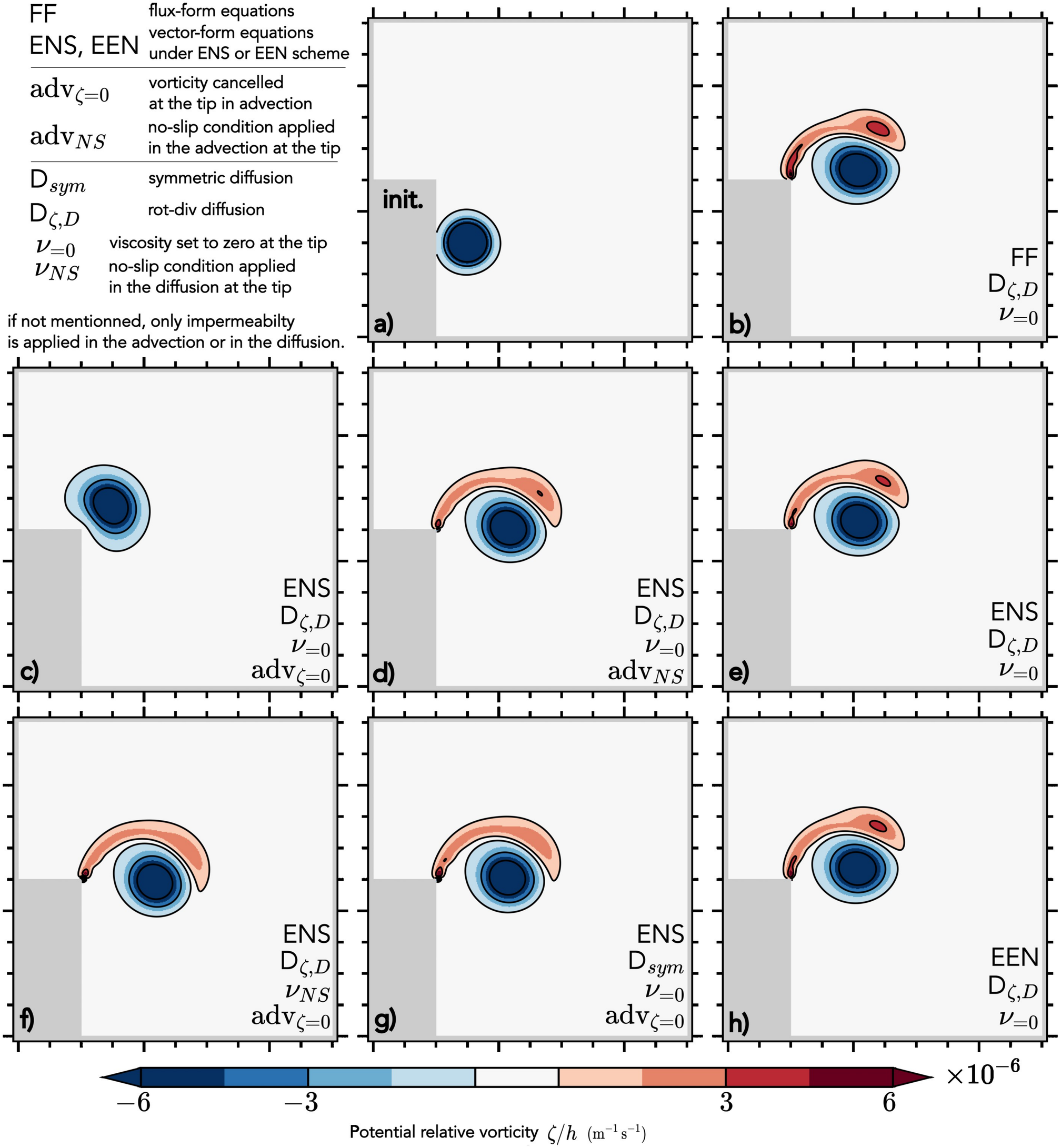

Figure B1.

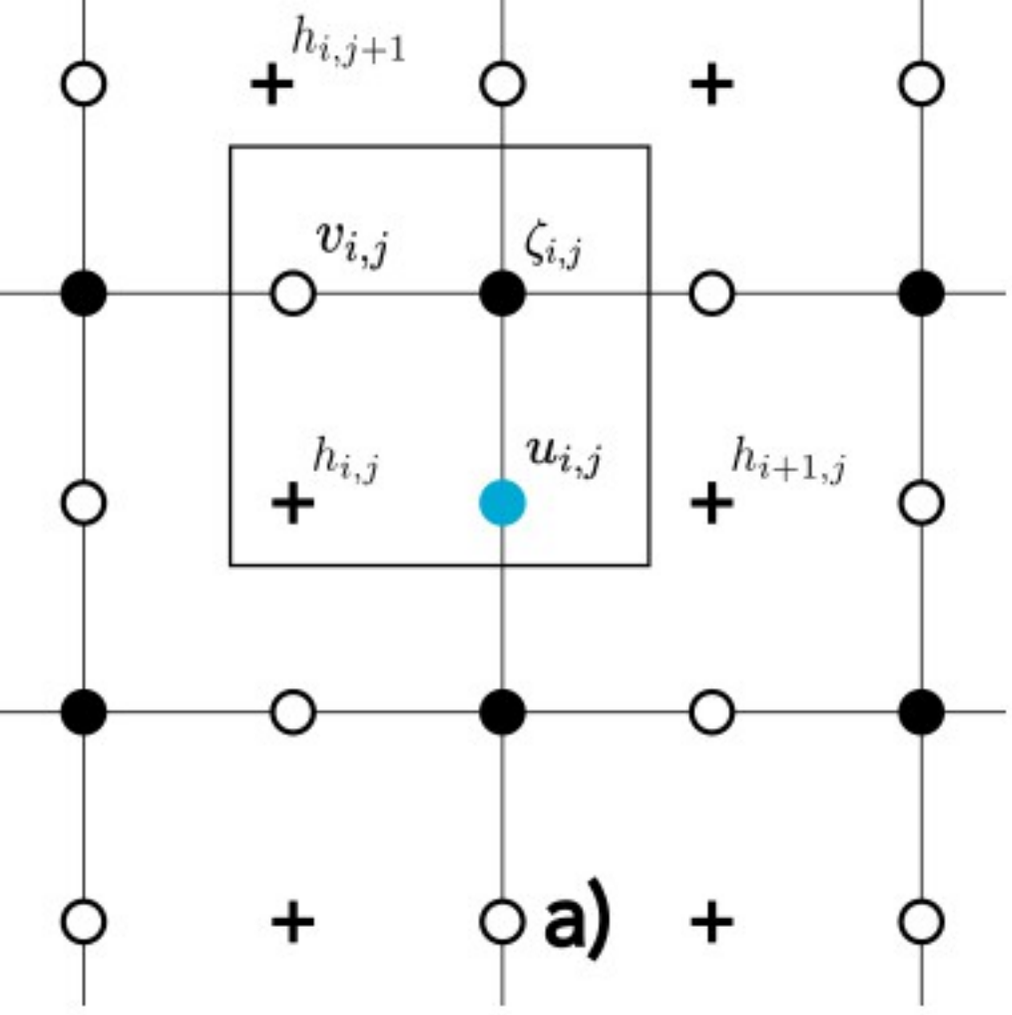
$h_{i,j+1}$
$v_{i,j}$
$\zeta_{i,j}$
$h_{i,j}$
$u_{i,j}$
$h_{i+1,j}$
a)

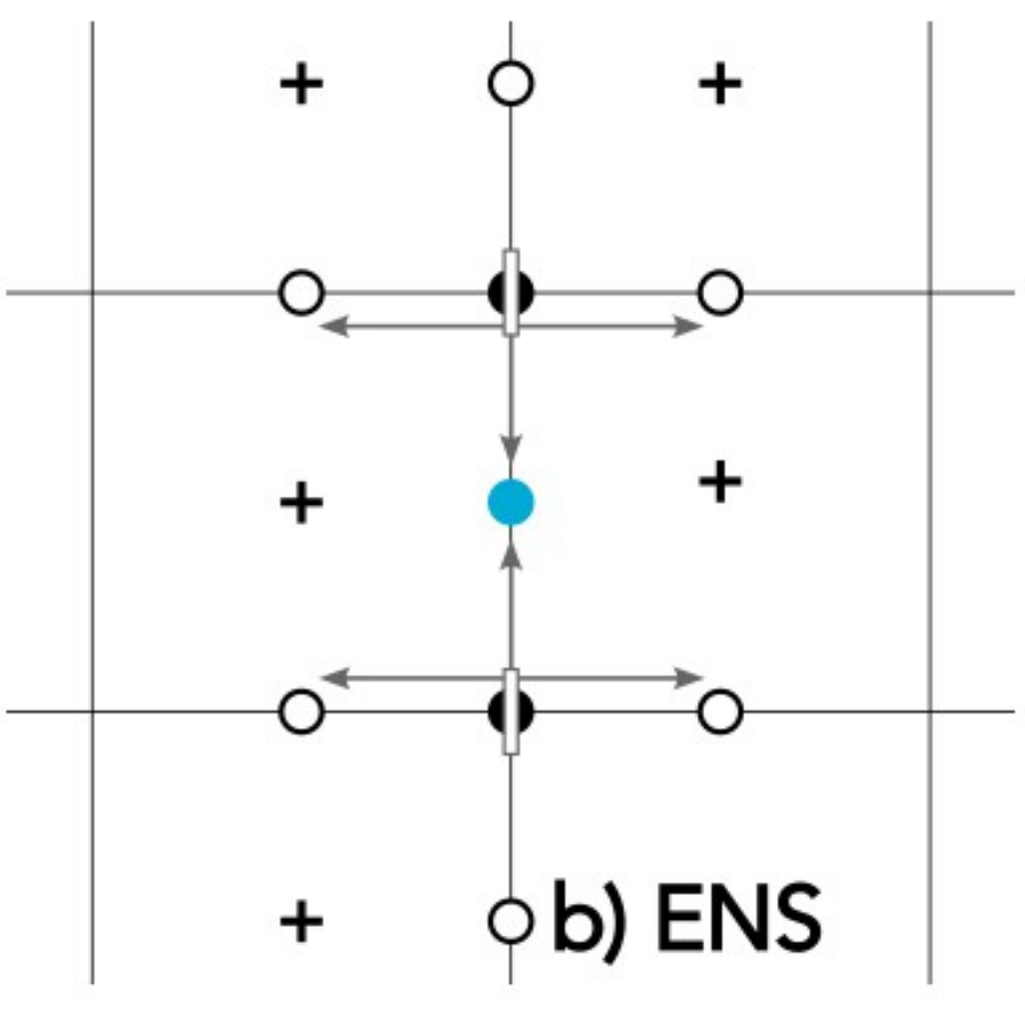
b) ENS

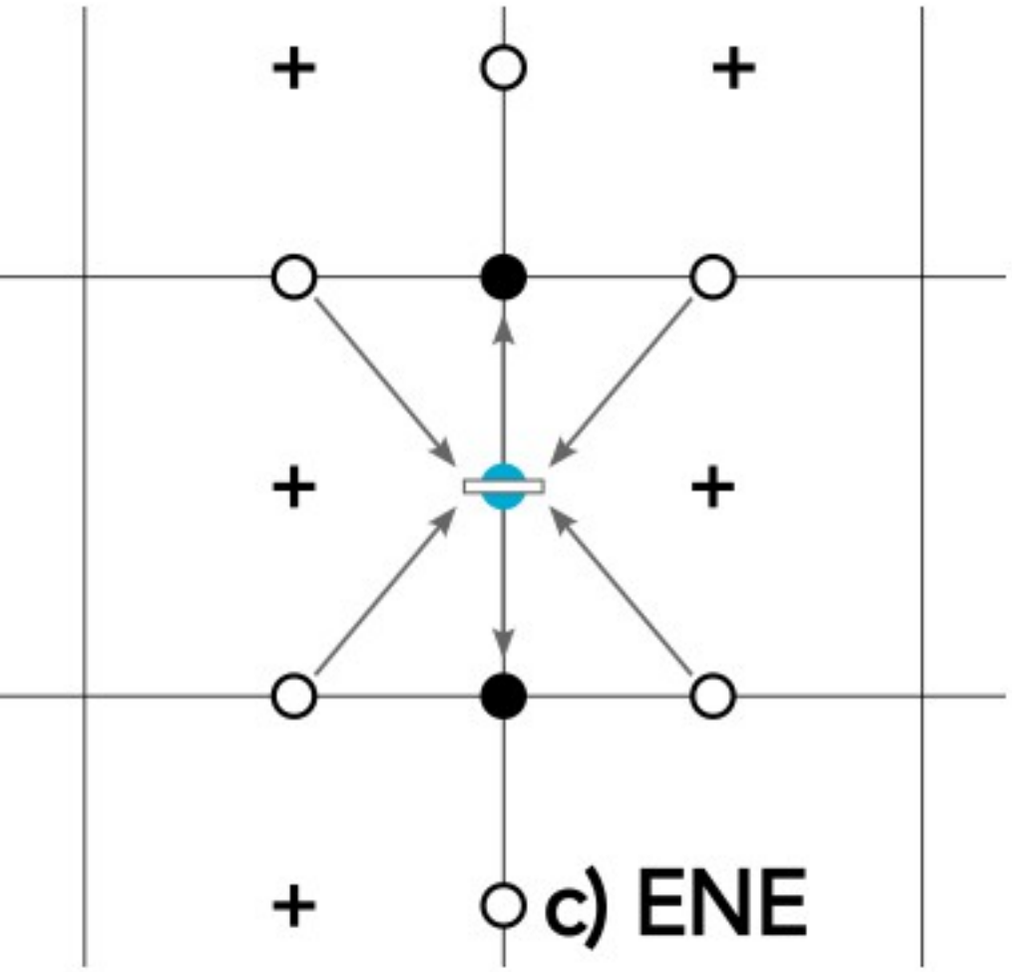
c) ENE

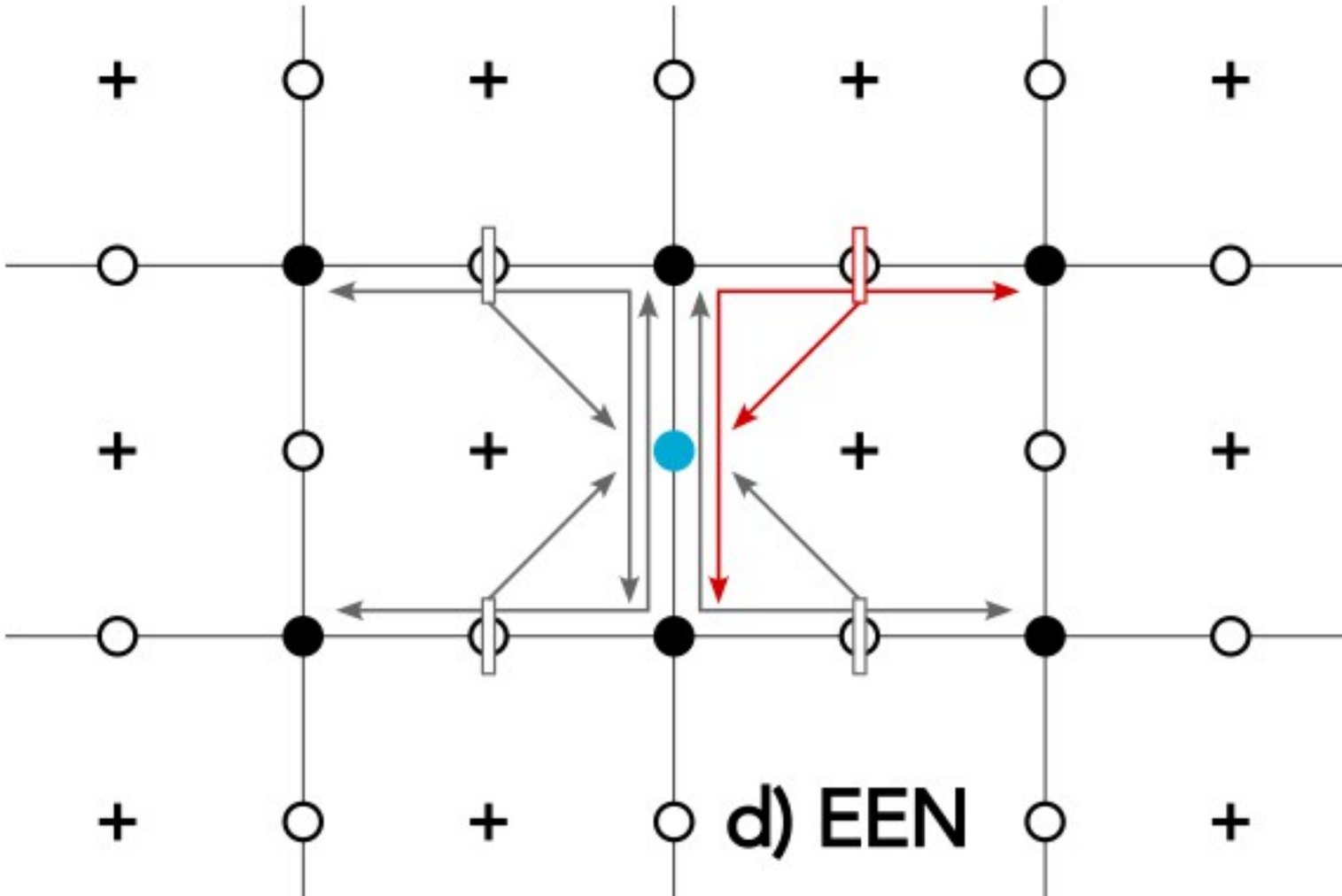
d) EEN